

## Laser-induced grating spectroscopy of alexandrite crystals

Guy D. Gilliland, Andrzej Suchocki,\* Keith W. Ver Steeg, and Richard C. Powell  
*Department of Physics, Oklahoma State University, Stillwater, Oklahoma 74078-0444*

Donald F. Heller

*Allied-Signal, Inc., Morristown, New Jersey 07960*

(Received 18 February 1988)

Four-wave-mixing techniques were used to establish and probe population gratings of  $\text{Cr}^{3+}$  ions in alexandrite crystals at temperatures between 10 and 300 K. The results were interpreted in terms of the interaction of the laser radiation with a two-level atomic system. They provide information about the characteristics of four-wave-mixing signals for this physical situation as well as being useful in characterizing the properties of energy transfer and dephasing within the ensemble of  $\text{Cr}^{3+}$  ions. The patterns of the transient four-wave-mixing signals are consistent with a model based on the pumping dynamics of ions in the mirror and inversion crystal-field sites. The variation of the signal intensity with laser power is strongly affected by beam depletion. The characteristics of exciton migration among  $\text{Cr}^{3+}$  ions in mirror sites were determined from the results of measuring the variation of the signal decay rate with grating spacing. The temperature dependences of the ion-ion interaction rate, the exciton-phonon scattering rate, and the diffusion coefficient were determined. These are found to be essentially the same for pumping into the  ${}^4T_2$  and  ${}^2E$  levels, but the effects of scattering from a grating of ions in inversion sites is much stronger for  ${}^4T_2$  pumping. The dephasing times for the atomic system were found from analyzing the variation of the signal intensity with grating spacing. For pumping into the  ${}^4T_2$  level the dephasing is dominated by radiationless decay processes. A model is presented for the decay channel that provides a theoretical explanation for the decay process which is consistent with the measured temperature and frequency dependences of the results as well as their variation with crystal-field strength. For pumping into the  ${}^2E$  level the dephasing is dominated by dephasing processes associated with the inhomogeneous linewidth of the transition.

### I. INTRODUCTION

Four-wave mixing (FWM) can be used as a spectroscopic technique by establishing excited-state, spatial population gratings in an ensemble of atoms or molecules.<sup>1-4</sup> We have recently applied this laser-induced-grating (LIG) spectroscopy method to the study of dynamical processes in several  $\text{Cr}^{3+}$ -doped laser crystals.<sup>5-8</sup> The results have been useful in characterizing the general properties of energy transfer, radiationless relaxation, and excited-state absorption in these materials under specific pumping conditions. The work reported here extends this study on one particular material, alexandrite, in two ways: The first involves the development of theoretical models to understand the properties of the LIG signal for this specific type of physical situation: the second involves additional investigations of energy transfer and radiationless relaxation, including both the use of different pumping conditions and the development of more rigorous theoretical models, which results in a more detailed understanding of the characteristics of these processes.

Alexandrite is an important, tunable, solid-state laser material consisting of  $\text{Cr}^{3+}$  ions substituted for  $\text{Al}^{3+}$  ions in a chrysoberyl host crystal,  $\text{BeAl}_2\text{O}_4$ .<sup>9</sup> The sample used in this investigation contained  $1.14 \times 10^{19} \text{ cm}^{-3}$   $\text{Cr}^{3+}$  ions. There are two nonequivalent crystal field sites for

the aluminum ions in the chrysoberyl lattice, one having mirror symmetry and one with inversion symmetry. Approximately 78% of the  $\text{Cr}^{3+}$  ions occupy mirror sites and 22% occupy inversion sites.<sup>10</sup> The optical spectroscopic properties of  $\text{Cr}^{3+}$  ions in each type of site have been reported previously.<sup>11-13</sup>

Previous LIG results on alexandrite demonstrated the ability to establish gratings in either mirror or inversion-site ions by pumping into the  ${}^4T_2$  levels of the ions in these two types of sites.<sup>5,8</sup> The gratings were found to be dominated by the difference in the dispersion contribution to the refractive index when the  $\text{Cr}^{3+}$  ions are in the excited state versus the ground state, with the contribution due to the difference in the ground- and excited-state absorption cross sections consistent with the results of direct excited-state absorption measurements.<sup>14</sup> The presence of exciton diffusion among the  $\text{Cr}^{3+}$  ions in mirror sites was observed below 150 K and the diffusion coefficient was found to increase as temperature was lowered. The dephasing times of the LIG signals were attributed to radiationless relaxation processes occurring after pumping into the  ${}^4T_2$  level and the rate of these processes was found to be different with different local crystal fields for the  $\text{Cr}^{3+}$  ions. Although these results demonstrated the general properties of laser-induced population gratings in alexandrite crystals, they left several unanswered questions about the observed transient and

equilibrium LIG signal characteristics and did not provide complete details of the exciton dynamics and radiationless relaxation processes in this material. Some of these questions are addressed in the following sections.

The detailed description of the LIG experimental setup was reported previously.<sup>8</sup> The two excitation beams of the same frequency were provided by either an argon-ion laser or an argon-ion-laser-pumped dye laser. A He-Ne laser was used for the probe beam. The dynamical response of the LIG signal was monitored by using a mechanical chopper to interrupt the pump beams while processing the signal beam with an EG&G Princeton Applied Research (PAR) signal averager. For measurements of the steady-state LIG signal, the probe beam was chopped and an EG&G PAR lock-in amplifier was utilized to improve the signal-to-noise ratio.

## II. EQUILIBRIUM POWER DEPENDENCE AND LIG SIGNAL TRANSIENTS

In order to fully understand the characteristics of signals observed in LIG spectroscopy involving population gratings, two theoretical models are required. The first involves the formalism describing the mixing of the four electromagnetic fields in the sample due to coupling through the nonlinear complex refractive index of the material. The second involves the formalism describing the pumping dynamics of the atomic system interacting with the laser beams. The laser pump beams interact with the atomic ensemble through a resonant electronic transition, thus changing the population distribution of atoms in different electronic levels. Since the complex refractive index of the system depends on the relative occupation of the various energy levels, this pumping provides the laser-induced modulation of the refractive index, which gives the coupling mechanism for the electric fields. The interference pattern of the two crossed laser pump beams results in a sine-wave spatial distribution of the excited-state population, and thus in a refractive index grating of the same shape. The model for the nonlinear interaction of the laser beams with the atomic system is essentially the same for all FWM applications. This is important in describing LIG spectroscopy results obtained under equilibrium pumping conditions such as the power dependence of the signal strength as described in this section and the dephasing time of the signal as described in Sec. IV. The additional model describing the pumping dynamics of the atomic system is required to explain the transient response of the LIG signal as described in this section and to characterize the effects of transient physical processes such as energy transfer or radiationless relaxation as described in the following two sections.

### A. Equilibrium power dependence

The pump power dependence of the FWM scattering efficiency is important in understanding the observed signals in LIG spectroscopy. The standard approach<sup>15,16</sup> in studying the dynamics of the transient grating formation is to model the system explicitly using the nonlinear wave equation which couples the electric fields through the

nonlinear susceptibility of the material. This theoretical approach to the FWM scattering efficiency predicts a quadratic dependence on pump power for laser intensities below the saturation intensity,  $I < I_s$ . Recently this theory was extended to apply to the geometrical situation used here.<sup>17</sup> The system is modeled as an ensemble of two-level atoms, and the fields are assumed to be plane waves. This is only an approximation to the actual case of focused Gaussian beams in a multilevel system, but the results predicted from this model are useful in understanding the spectral and FWM dynamics. This model and the model of Abrams and Lind<sup>15</sup> start with the same assumptions, but the theoretical development of the two models differ.

For a two-level system the polarization can be expressed as

$$P(E_0 + \Delta E) = e^{i\omega t} X(E_0) \times \left[ E_0 + \Delta E - \frac{E_0^2 \Delta E^* + |E_0| (\Delta E)^2}{I_s + |E_0|^2} \right], \quad (1)$$

where

$$X(E) = -2(\alpha_0/k)[(i + \delta)/(1 + \delta^2 + |E/E_s|^2)] \quad (2)$$

$\delta$  is the normalized detuning from line center,  $\alpha_0$  is the line-center small-signal attenuation coefficient,  $E_s$  is the saturation field,  $I_s$  is the saturation intensity,  $E_0 = E_a + E_b$ , and  $\Delta E = E_p + E_s$ .  $E_a$  and  $E_b$  represent the write beams,  $E_p$  represents the probe beam, and  $E_s$  represents the signal beam. Assuming plane waves for all of the fields and equal intensities for the write beams ( $I_a = I_b$ ), using the slowly varying envelope approximation, and solving the wave equation

$$\nabla^2 \mathbf{E} + \frac{\epsilon}{c^2} \frac{\partial^2 \mathbf{E}}{\partial t^2} = -\frac{4\pi}{c^2} \frac{\partial^2 \mathbf{P}^{NL}}{\partial t^2}, \quad (3)$$

where

$$\mathbf{P}^{NL} = \chi \mathbf{E} \quad (4)$$

leads to two coupled equations for the fields. Solving these equations yields an expression for the scattering efficiency given by<sup>17</sup>

$$\eta = \frac{(I/I_s)^2 (1 + 2I/I_s)^2 \exp[2\alpha_0 L / (1 + \delta^2)]}{\{[(1 + 2I/I_s) - 2(I/I_s)^2] (\sec\theta - 1)\}^2} \times \{ \exp(-2\xi_R L) + \exp(-2\xi_R L \sec\theta) - 2 \exp[-\xi_R (1 + \sec\theta)L] \cos[\xi_I (1 - \sec\theta)L] \}, \quad (5)$$

where

$$\xi = \xi_R + i\xi_I = \alpha_0 \frac{1 - i\delta}{1 + \delta^2} \frac{[1 + 2I/I_s - 2(I/I_s)^2]}{[(1 + 2I/I_s)^2 - 4(I/I_s)^2]^{3/2}}. \quad (6)$$

Equation (5) can be simplified somewhat, if  $|\xi L|$  is small and  $\theta$  is not very large, yielding<sup>17</sup>

$$\eta = \frac{\alpha_0^2 / (1 + \delta^2) \{ (I/I_s)^2 (1 + 2I/I_s)^2 L^2 \exp(-2\xi_R L) \exp[2\alpha_0 L / (1 + \delta^2)] \}}{[(1 + 2I/I_s)^2 - 4(I/I_s)^2]^3} [1 + \xi_R L (1 - \sec\theta)] . \quad (7)$$

For  $I \ll I_s$ , this equation shows that the FWM scattering efficiency depends quadratically upon the write-beam power. In both equations  $\eta$  decreases with increasing  $\theta$ .

Figure 1 shows the FWM relative scattering intensity as a function of the laser power in each of the write beams for direct excitation of the  $2\bar{A}$  sublevel of the split  ${}^2E$  state. The LIG was formed by crossing two laser beams from an argon-ion-pumped jet dye laser using DCM [4-(dicyanomethylene)-2-methyl-6-(*p*-dimethylamino-styryl)-4*H*-pyran] dye tuned to 677.8 nm. Using the measured lifetime, absorption cross section, and absorption wavelength for this transition (2.3 ms,  $8.5 \times 10^{-20}$  cm<sup>2</sup>, and 677.8 nm, respectively) the saturation intensity is approximately 1500 W/cm<sup>2</sup>. The dashed line in Fig 1 is the best fit to the data using Eq (7) with  $I_s = 1500$  W/cm<sup>2</sup>. The theoretical curve has a slope of two, while the data has a less-than-quadratic dependence on write-beam power. The solid line in the figure is the best fit to the data using the full scattering efficiency expression, Eq. (5), with the same value for  $I_s$ . The theoretical fit to the data is quite good, showing a departure from the quadratic power dependence at high powers.

The difference between the two expressions used to fit the data in Fig. 1 is a result of the simplifying assumption made in deriving Eq. (7) from Eq. (5). The assumption made is that  $|\xi L|$  is small. Since the absorption line excited is quite narrow ( $\approx 1$  cm<sup>-1</sup>) and the laser linewidth is approximately of the same width (0.7 cm<sup>-1</sup>), it can be assumed that the imaginary part of  $\xi$  is zero since the normalized detuning parameter is zero.  $\xi_R$  represents the laser-induced change in the absorption coefficient. The results presented above imply that the laser induced change in the absorption coefficient is not negligible for

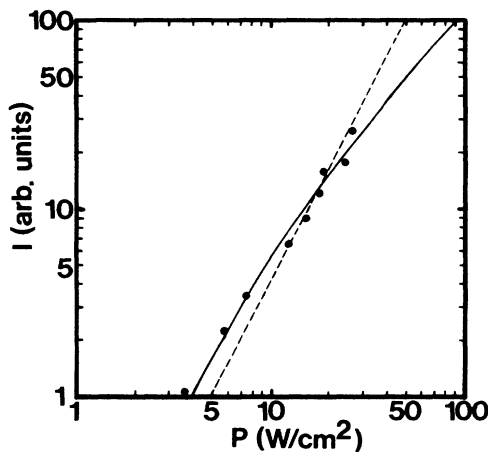


FIG. 1. FWM relative scattering intensity of Cr<sup>2+</sup> ions in mirror sites in alexandrite as a function of the laser power of each write beam for direct excitation of the  $2\bar{A}$  sublevel of the  ${}^2E$  state at 50 K. The dashed and solid lines represent the theoretical fits from Eqs. (7) and (5), respectively.

these experimental conditions. This causes additional beam depletion which is evident in the experimental results.

Experimental measurements of the power dependence of the FWM signal pumping into the  ${}^4T_2$  level of the mirror sites have been done previously.<sup>5,8</sup> A slight saturation is evident in the data. This departure from quadratic power dependence is also a result of the laser-induced change in the absorption coefficient and not a purely saturation effect since the power of the write beams was much less than the saturation intensity.

### B. Transient LIG signal patterns

Transient FWM signals have many unique features that distinguish them from steady-state FWM signals. Abrams and Lind<sup>15</sup> have studied steady-state FWM processes theoretically, and Silberberg and Bar-Joseph<sup>18</sup> have extended their steady-state solutions to the treatment of the transient FWM response of a saturable absorber. As mentioned earlier, the FWM signal in alexandrite crystals is a result of scattering of the probe beam from a laser-induced grating that is predominantly dispersive. Although the results of Abrams and Lind<sup>15</sup> apply to absorption gratings, dispersion gratings, or a mixed grating, the theoretical treatment of the time evolution of the FWM signal in the presence of all three laser beams has only been applied to pure absorption gratings.<sup>18-20</sup> In this section the theoretical treatment of the time evolution of the FWM signal is extended to the case of a mixed grating, and the results are used to analyze the transient LIG signal from Cr<sup>3+</sup> population gratings of ions in both types of crystal-field sites in alexandrite.

Assuming a three-level atomic system, where the relaxation between the level directly excited and the metastable level is fast and the lifetime of the metastable level is relatively long, the rate equation for the ground-state population density is

$$\frac{ds_0}{dt} = -(\sigma I / \hbar\omega) s_0 + (S - s_0) / \tau . \quad (8)$$

In Eq. (8)  $\sigma$  is the absorption cross section,  $I$  is the laser intensity of each write beam of frequency  $\omega$ ,  $S$  is the total population of ions, and  $\tau$  is the lifetime of the metastable level. This model adequately describes the dynamics of Cr<sup>3+</sup> ions when the  ${}^4T_2$  level is pumped, followed by a fast nonradiative decay to the  ${}^2E$  level which has a relatively long lifetime (2.3 ms at 12 K). The solution of Eq. (8) assuming a step function for the laser intensity with the initial condition that  $I(t=0)=0$  is

$$\frac{s_0(t)}{S} = \frac{1 + (I/I_s) \exp[-(t/\tau)(1 + I/I_s)]}{1 + I/I_s} , \quad (9)$$

where  $I_s = (\hbar\omega / \sigma\tau)$  is the saturation intensity. It is important to note that the time development of the system

depends upon the saturation intensity and write-beam intensity.

Following the treatment of Abrams and Lind<sup>15</sup> in which the four fields, two write beams, the probe beam, and the signal beam, are assumed to be plane waves, and the interaction between the fields takes place through the complex susceptibility  $X$  the interaction is expressed in terms of the wave equation, Eq. (3). The complex susceptibility can be expressed in terms of the complex index of refraction  $\hat{n} = \bar{n} + i(\alpha/2k)$  as

$$X = \bar{n}^2 - 1 - \alpha^2/4k^2 + i(\alpha\bar{n}/k), \quad (10)$$

where  $k$  is the magnitude of the wave vector of the write beams,  $\bar{n}$  is the index of refraction, and  $\alpha(t) = \sigma s(t)$  is the time-dependent absorption coefficient. Using the nonlinear index of refraction

$$\bar{n}(t) = n + s_2(t)(\Delta n), \quad (11)$$

where  $n$  is the normal index of refraction, and  $\Delta n$  is the change in the index of refraction due to the presence of

an ion in the excited state, it is evident that both the real and imaginary parts of the susceptibility and hence the FWM interaction are time dependent. The expression for the FWM scattering intensity is<sup>15</sup>

$$\eta = |\kappa \sin(\Delta L)|^2 / |\Delta \cos(\Delta L) + \Upsilon_R \sin(\Delta L)|^2 \quad (12)$$

where  $\Delta = (|\kappa|^2 - \Upsilon^2)^{1/2}$ ,  $L$  is the length of the sample,  $\Upsilon_R$  is the real part of  $\Upsilon$ , where

$$\Upsilon(t) = (k/2i)(X + I_s P dX/dI), \quad (13)$$

$$\kappa^*(t) = \frac{1}{2} k I_s P dX/dI, \quad (14)$$

and  $P = 4(I/I_s) \cos^2 \theta$ .  $\theta$  is the angle between the two write beams. It is important to note that the FWM process is a result of the term  $dX/dI$ , so that if  $X$  is independent of  $I$  then there is no FWM signal generated. Because only the real part of  $\Upsilon$  appears in the expression for  $\eta$ , only the terms  $\Upsilon_R$ ,  $\kappa_R$ , and  $\kappa_I$  need to be calculated. Using Eqs. (10)–(14) the absorption and coupling coefficients become

$$\begin{aligned} \Upsilon_R(t) = \frac{1}{2} \left[ S(\Delta n)n + S[n\sigma + S(\Delta n)\sigma] \frac{1 + P \exp[-t/\tau(1+P)]}{1+P} \right. \\ \left. + SP[n\sigma + S(\Delta n)\sigma] \frac{[1 - t/\tau P(1+P)] \exp[-t/\tau(1+P)] - 1}{(1+P)^2} \right. \\ \left. - 2n^2(\Delta n) \frac{\sigma \{1 + P \exp[-t/\tau(1+P)]\} / (1+P) \{1 - t/\tau P(1+P) \exp[-t/\tau(1+P)] - 1\}}{(1+P)^2} \right. \\ \left. - n^2(\Delta n) \sigma \frac{\{1 + P \exp[-t/\tau(1+P)]\}^2}{(1+P)^2} \right], \quad (15) \end{aligned}$$

$$\begin{aligned} \kappa_R(t) = \frac{1}{2} k P \left[ S[-2S(\Delta n)^2 - 2n(\Delta n)] \frac{[1 - t/\tau P(1+P)] \exp[-t/\tau(1+P)] - 1}{(1+P)^2} \right. \\ \left. + S^2[2(\Delta n)^2 - \sigma^2/2k^2] \frac{\{1 + P \exp[-t/\tau(1+P)]\} / (1+P) \{1 - t/\tau P(1+P) \exp[-t/\tau(1+P)] - 1\}}{(1+P)^2} \right], \quad (16) \end{aligned}$$

$$\begin{aligned} \kappa_I(t) = -\frac{1}{2} P \left[ S[n\sigma + S(\Delta n)\sigma] \frac{[1 - t/\tau P(1+P)] \exp[-t/\tau(1+P)] - 1}{(1+P)^2} \right. \\ \left. - 2S^2\sigma(\Delta n) \frac{\{1 + P \exp[-t/\tau(1+P)]\} / (1+P) \{1 - t/\tau P(1+P) \exp[-t/\tau(1+P)] - 1\}}{(1+P)^2} \right]. \quad (17) \end{aligned}$$

Equations (15)–(17) have contributions from an absorption grating, a dispersion grating, and a mixed grating.

Previous theoretical work<sup>15–20</sup> has shown that for small write-beam intensities the LIG scattering efficiency increases quadratically with pump intensity, but that it saturates at higher intensities. In the steady state, the maximum LIG signal is obtained for  $I$  approximately equal to  $I_s$ . However, the transient LIG signal can be much larger than the steady-state LIG signal. When  $I < I_s$  the LIG is predicted to increase monotonically to its steady-state value, but when  $I \geq I_s$  the transient LIG signal peaks at short times at a value greater than the steady-state LIG signal and then decays to the steady-

state value. The temporal behavior of the transient LIG signal for the case of a mixed or purely dispersive grating is similar to the case of a pure absorption grating.

Alexandrite is an ideal candidate for studying the effects of saturation on the spectral dynamics. The parameter  $P$  directly affects the time dependence of the LIG signal, and  $P$  is a function of several LIG variables and constants of the material including the lifetime of the excited state. The lifetime of the mirror-site ions ranges from 2.3 ms to 290  $\mu$ s at temperatures of 12 to 300 K, whereas the lifetime of the inversion sites ranges from 63 to 44 ms over the same temperature range.<sup>11,12</sup> Another method of varying  $P$  is by changing the period of the

grating or the angle between the write beams. For these reasons it is possible to vary the saturation intensity, and hence the parameter  $P$  which appears in the expressions for the absorption coefficient and coupling constants.

The transient LIG signal for the inversion-site ions shows a transient peak which is dependent on several parameters. Figure 2 shows the normalized transient LIG signal at 30 K for various powers of the write beams. The data was normalized because it is very difficult to determine the absolute scattering efficiency, and the shape of the FWM transient is the only thing needed for the theoretical fits. The solid line is the theoretical fit to the data using Eqs. (12) and (15)–(17) and treating  $\sigma$  and  $\Delta n$  as adjustable parameters. Figure 3 shows the transient FWM signal for several temperatures and write beam crossing angles at constant write beam laser power, along with the theoretical fits. The theoretical fits accurately

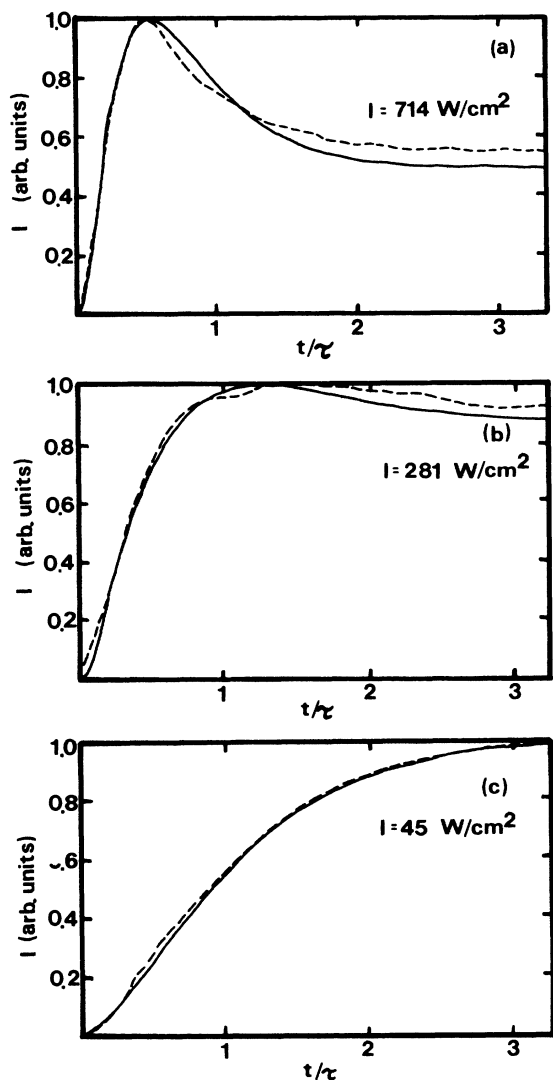


FIG. 2. Normalized transient LIG signal for  $\text{Cr}^{2+}$  ions in inversion sites as a function of time at 30 K for various write-beam powers: (a)  $714 \text{ W/cm}^2$ , (b)  $281 \text{ W/cm}^2$ , (c)  $45 \text{ W/cm}^2$ . The dashed lines represent the data and solid lines represent the theoretical fits using Eq. (12).

model the transient LIG signal as a function of temperature, crossing angle, and laser power. The temperature dependence is a result of the temperature dependence of the excited-state lifetime. The values obtained for  $\sigma$  and  $\Delta n$  from these fits are  $0.5 \pm 0.1 \times 10^{-20} \text{ cm}^2$  and  $2.0 \times 10^{-23} \text{ cm}^3$ , respectively. Using these values, the saturation intensity is  $900 \text{ W/cm}^2$ .

This value for the absorption cross section for the inversion site ions at 488 nm is consistent with the upper limit of  $1.0 \times 10^{-20} \text{ cm}^2$  obtained from absorption measurements.<sup>11–13</sup> It is difficult to distinguish the inversion-site absorption contribution from the mirror-site absorption since the emission and absorption properties of alexandrite are dominated by the mirror-site ions.<sup>9</sup>

In order to compare the laser-induced change in the index of refraction obtained here with the results of other measurements,<sup>5,8</sup> it is necessary to calculate the steady-state value of  $\Delta n$ , denoted by  $\Delta n_{ss}$ , and given by

$$\Delta n_{ss} = \Delta n [S(I/I_s)/(1 + I/I_s)] . \quad (18)$$

For  $I = 100 \text{ W/cm}^2$ ,  $\Delta n_{ss}$  equals  $5.0 \times 10^{-6}$ . This is an order of magnitude smaller than the value obtained from other measurements<sup>5,8</sup> of  $\Delta n_{ss}$ , but all of the data are consistent with the statement given earlier that the gratings formed are dispersion gratings. It should be noted that the steady-state value of the theoretical signal intensity is smaller than the experimental value at large excitation intensities. This contributes to the discrepancy in the values of  $\Delta n$ .

The same type of measurements were repeated for the mirror-site ions. The  ${}^4T_2$  level of the mirror site ions was pumped by an argon-ion pumped dye laser with Rhodamine 6G as a dye. The results of the measurements are similar to the low-power measurements for the inversion site ions. There is no transient peak formed, and the signal increases monotonically to its steady state value. This can be understood, in contrast to the inversion site results, as a result of two things. First, the laser output from the ring dye laser was less than the maximum power output of the argon-ion laser at 488 nm by a factor of 3. Second, the saturation intensity for the mirror-site ions is greater than the saturation intensity of the inversion-site ions. This is a result of the difference in lifetimes and absorption cross sections. The saturation intensity for the mirror-site ions is estimated to be approximately  $1200 \text{ W/cm}^2$  at 12 K and increases with temperature due to the decrease in the lifetime with temperature. Therefore, it is not surprising that no transient peak was observed in the mirror-state LIG signal.

### III. ENERGY TRANSFER

Laser-induced grating spectroscopy has been used to characterize the properties of long-range energy migration among  $\text{Cr}^{3+}$  ions in mirror and inversion sites in alexandrite.<sup>5,8</sup> The previous measurements were performed using either an argon-ion laser or argon-ion-pumped ring dye laser with Rhodamine 6G dye for the pump beams. Both of these are resonant with the  ${}^4T_2$  absorption band of the mirror or inversion-site ions. These LIG measurements were extended in the work described

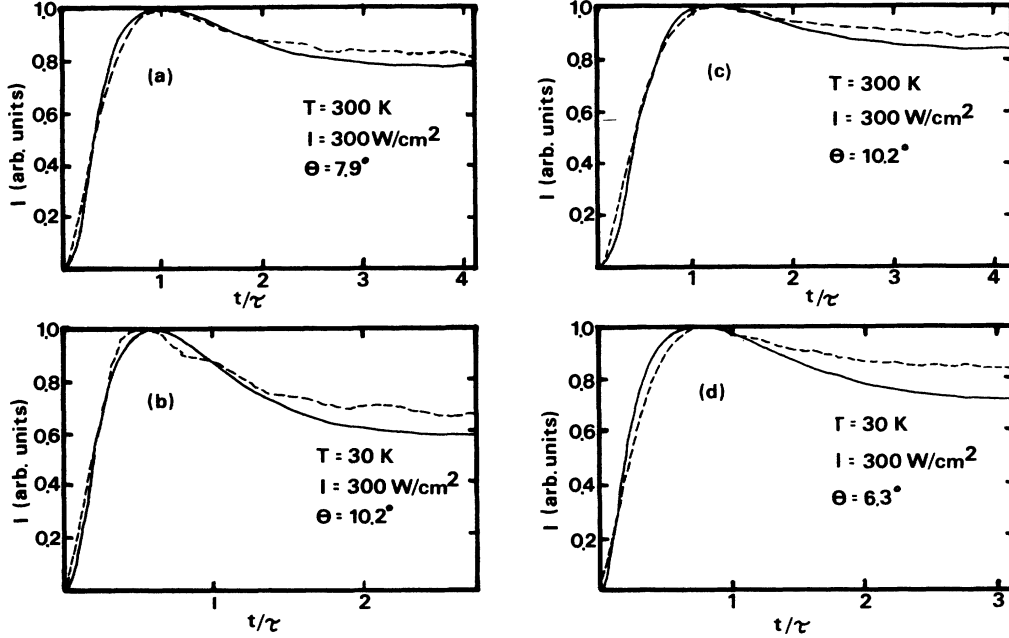


FIG. 3. Normalized transient LIG signal for  $\text{Cr}^{3+}$  ions in inversion sites for several temperatures and write-beam crossing angles at constant write-beam laser power. (a)  $T = 300$  K and  $\theta = 7.9^\circ$ , (b)  $T = 30$  K and  $\theta = 10.2^\circ$ , (c)  $T = 300$  K and  $\theta = 10.2^\circ$ , and (d)  $T = 30$  K and  $\theta = 6.3^\circ$ . The dashed lines represent the data and the solid lines represent the theoretical fits using Eq. (12).

here to the case of direct excitation into the  $2\bar{A}$  sublevel of the  ${}^2E$  state of the mirror-site ions. The population grating in the  ${}^2E$  state was established by crossing two laser beams from an argon-ion-pumped jet dye laser using DCM dye tuned to 677.8 nm. In addition experiments were performed using crossed laser beams from both the argon-ion laser and argon-ion-pumped ring dye laser to simultaneously establish gratings in both mirror and inversion site ions in order to determine the effects of the dual gratings on the LIG signals.

It was reported earlier<sup>5</sup> that the FWM signal decay kinetics were nonexponential for excitation into the  ${}^4T_2$  level of the mirror-site ions. The long-time portion of the decay curves was found to approach the decay time expected for an inversion-site grating and was attributed to an inversion-site grating formed as a result of weak inversion-site absorption. In the data presented below for direct excitation of the  ${}^2E$  level of the mirror-site ions no long-time tail is evident.

In order to use LIG spectroscopy to study energy migration among  $\text{Cr}^{3+}$  ions the grating decay rate is measured as a function of the grating spacing.<sup>21,22</sup> The grating spacing is related to the total crossing angle of the write beams by

$$\Lambda = \lambda / [2 \sin(\theta/2)], \quad (19)$$

where  $\theta$  is the total crossing angle between the write beams and  $\lambda$  is the write-beam wavelength. As the grating spacing decreases energy migration from the peak to the valley of the grating becomes more efficient in destroying the LIG. For the initial conditions relevant to this experimental case, the time dependence of the normalized transient-grating signal in the presence of energy

migration processes is given by<sup>23</sup>

$$I_s(t) = \exp(-2t/\tau) \left[ J_0(bt) \exp(-\alpha t) + \alpha \int_0^\infty du \exp[-\alpha(t-u)] \times J_0(b(t^2-u^2)^{1/2}) \right]^2, \quad (20)$$

where  $\tau$  is the fluorescence lifetime,  $\alpha$  is the exciton scattering rate,  $J_0$  is the Bessel function of order zero, and  $b$  is given by

$$b = 4V \sin[(2\pi a/\lambda) \sin(\theta/2)], \quad (21)$$

where  $V$  is the nearest-neighbor ion-ion interaction rate,  $a$  is the average distance between active ions,  $\lambda$  is the excitation wavelength and  $\theta$  is the crossing angle between the write beams (both in air). The exciton dynamics can be characterized by these parameters in terms of the diffusion coefficient, the mean free path, the diffusion length, the coherence parameter, and the number of sites visited between scattering events given by

$$D = 2V^2 a^2 / \alpha, \quad (22)$$

$$L_m = \sqrt{2} Va / \alpha, \quad (23)$$

$$L_d = (2D\tau)^{1/2}, \quad (24)$$

$$\zeta = b / \alpha, \quad (25)$$

$$N_s = L_m / a, \quad (26)$$

respectively.

### A. Results for ${}^4T_2$ excitation

For the grating formed by excitation into the  ${}^4T_2$  level of the mirror-site ions the decay of the signal is nonexponential. The initial part of the decay is consistent with the predicted decay of a mirror-site grating and the long-time part of the decay is consistent with the predicted decay of an inversion site grating. The angular dependence of the grating decay pattern shows that at large crossing angles the long-time decay is very weak or no longer present. This is shown in Fig. 4.

The concentration of inversion-site  $\text{Cr}^{3+}$  ions in the sample is  $2.5 \times 10^{18} \text{ cm}^{-3}$ . Assuming a uniformly random distribution of ions, this implies an average separation of 457 nm between inversion-site  $\text{Cr}^{3+}$  ions. The angles used in the measurements ranged from  $2^\circ$  to approximately  $28^\circ$ . This gives grating spacings ranging from 1.2 to  $16 \mu\text{m}$ . The spatial dependence of the grating is given by

$$n(x,0) \approx [\cos(k_g x) + 1], \quad (27)$$

where  $k_g = 2\pi/\Lambda$  is the grating  $k$  vector, and  $n(x,0)$  is the exciton concentration at  $t=0$ . The characteristic width of a grating peak is  $\Lambda$ . For a grating spacing of  $16 \mu\text{m}$  this implies a linear density of 35 inversion-site  $\text{Cr}^{3+}$  ions per grating peak. For a grating spacing of  $1.2 \mu\text{m}$  the linear density of inversion-site  $\text{Cr}^{3+}$  ions is 2.6 per grating peak. This clearly shows, under the above assumptions, that the number of inversion-site ions per peak of the grating decreases with increasing crossing angle (decreasing grating spacing), and as a result, the inversion-site grating signal decreases in intensity with increasing crossing angle.

In order to conclusively establish that the observed long-time part of the decay patterns is a result of the

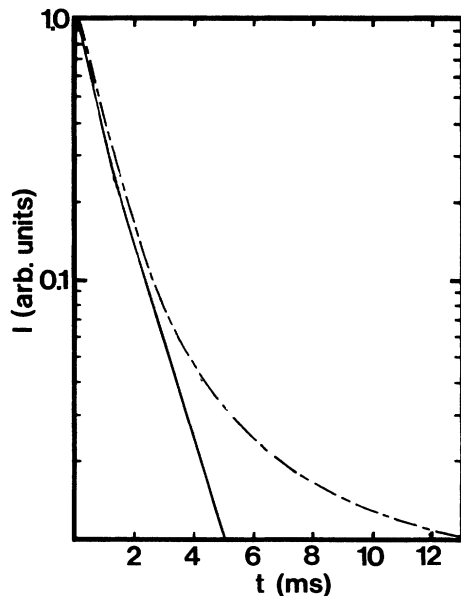


FIG. 4. The LIG signal decay for excitation of the mirror-site  $\text{Cr}^{2+}$  ions into the  ${}^4T_2$  level at 30 K at two different write-beam crossing angles. The dashed line is  $\theta = 3.5^\circ$ ; the solid line is  $\theta = 23^\circ$ .

simultaneous formation of an inversion-site grating along with the mirror site grating, the following experiment was performed. A mirror site grating and an inversion site grating were formed simultaneously in the same region in the sample by using two different sets of pump laser beams as described earlier. A single He-Ne beam was used to probe the dual grating. Because the fringe spacings of the two gratings are not exactly the same due to the different laser frequencies used to write the gratings, it was necessary to keep the crossing angle between the two sets of overlapping write beams very small so that a single probe beam can approximately match the Bragg condition for both gratings simultaneously. The decay kinetics of the resulting dual grating were measured by chopping both sets of pump beams and recording the dual LIG signal. The results are shown in Fig. 5. The decay pattern is similar to the small-angle decay pattern for  ${}^4T_2$  pumping, shown in Fig. 4. This confirms that the long-time part of the decay for  ${}^4T_2$  pumping is due to the presence of an inversion-site grating.

### B. Results for ${}^2E$ excitation

The FWM signal decay kinetics of the mirror-site grating formed by direct excitation of the  ${}^2E$  level were also found to be dependent on the grating spacing and temperature. Several approaches<sup>22-24</sup> have been used to theoretically analyze the transient grating kinetics in the presence of energy transfer. Kenkre<sup>23,24</sup> has treated the case for the effects of partially coherent exciton migration, with the initial conditions relevant to the experiments described here. His results are derived from the generalized master equations using the assumption that the initial density matrix for the system is diagonal. This is the situation encountered in systems with localized exciton states or systems containing complete randomness between the phases of the exciton wave functions. The

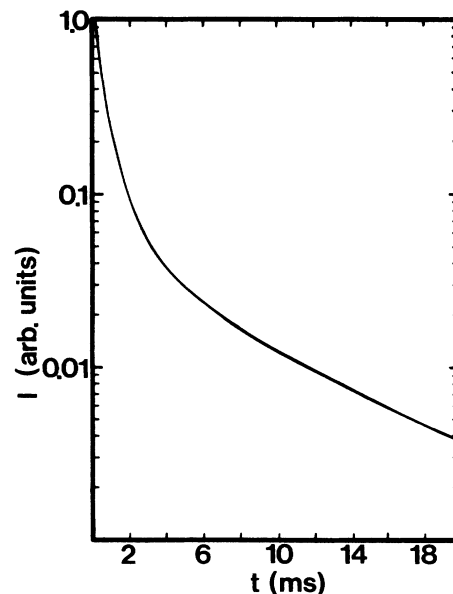


FIG. 5. Dual-grating decay kinetics at 30 K and a write-beam crossing angle of  $1.39^\circ$ .

TABLE I. Energy migration parameters at 25 K.

$V$ (sec $^{-1}$ )	$1.22 \times 10^6$
$\alpha$ (sec $^{-1}$ )	$0.2 \times 10^6$
$D$ (cm $^2$ sec $^{-1}$ )	$3.02 \times 10^{-8}$
$L_m$ (cm)	$3.88 \times 10^{-7}$
$L_d$ (cm)	$1.18 \times 10^{-5}$
$N_s$	8.63
$\zeta$ ( $\theta=5^\circ$ )	$3.7 \times 10^{-3}$

later case is exactly the situation encountered here. At low temperatures the population of excited  $\text{Cr}^{3+}$  ions is predominantly in the  $\bar{E}$  sublevel of the  ${}^2E$  state, whereas the excitation is into the  $2\bar{A}$  sublevel. A correlation exists between different  $\text{Cr}^{3+}$  sites in the  $2\bar{A}$  sublevel immediately after the pump photons are absorbed, since the excitation wavelength spans many  $\text{Cr}^{3+}$  sites. However, any dephasing mechanism, such as nonradiative processes between the  $\bar{E}$  and  $2\bar{A}$  sublevels or phonon scattering processes, will result in a loss of this correlation between sites. Therefore, the theory of Kenkre<sup>23</sup> is ideally suited to this system. The dephasing issue will be discussed later in this paper.

For  ${}^2E$  excitation there is no inversion-site contribution to the LIG signal, and therefore the decay kinetics of the signal can unambiguously be analyzed in terms of energy migration only among mirror site  $\text{Cr}^{3+}$  ions. Equation (20) was used to fit the slightly nonexponential LIG decay kinetics treating  $b$  and  $\alpha$  as adjustable parameters. The LIG decay kinetics at each temperature and several different grating spacings were used to characterize the exciton migration at that specific temperature. The pertinent parameters are listed in Table I.

Figure 6 shows the temperature dependence obtained for the scattering rate  $\alpha$ . The solid line is the best fit to the data using the expression

$$\alpha = C_1 T^{C_2} \quad (28)$$

with  $C_1 = 0.02 \times 10^6 \text{ sec}^{-1}$  and  $C_2 = 0.75 \pm 0.08$ .

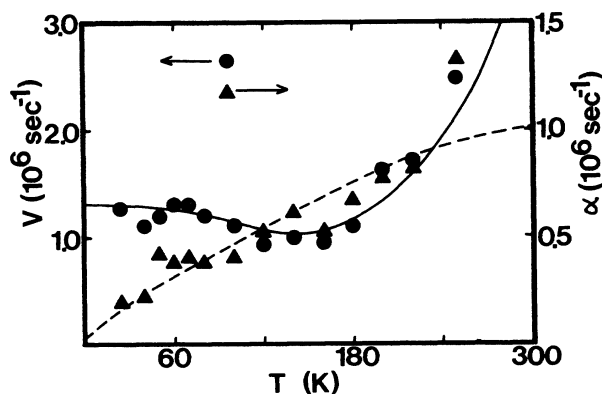


FIG. 6. The temperature dependence obtained for the scattering rate and the ion-ion interaction rate for direct excitation of the  ${}^2E$  level of the  $\text{Cr}^{3+}$  ions in mirror sites. The solid line is the theoretical fit to the ion-ion interaction rate using Eq. (28), and the dashed line is the theoretical fit to the scattering rate using Eq. (29).

Figure 6 also shows the temperature dependence of the ion-ion interaction rate. For resonant energy migration in the  $R_1$  zero-phonon line originating on  ${}^2E$ , the ion-ion interaction rate is proportional to the spectral overlap integral of the  $R_1$  absorption and emission transitions, and the intrinsic decay rate of the  ${}^2E$  level.<sup>25</sup> This can be expressed as

$$V = C_3 \tau^{-1} / \Delta\nu, \quad (29)$$

where  $\Delta\nu$  is the FWHM of the zero-phonon line, and it was assumed that the zero-phonon lineshape was Gaussian. The temperature dependencies of  $\tau^{-1}$  and  $\Delta\nu$  have been measured for the  $R_1$  mirror site zero-phonon line in alexandrite.<sup>11</sup> The solid line in Fig. 6 is the best fit to the measured ion-ion interaction rate using Eq. (29) and the measured values of  $\tau^{-1}$  and  $\Delta\nu$ .

Using Eq. (22) the diffusion coefficient can be calculated from  $V$  and  $\alpha$  in terms of  $a$ . The magnitude of the diffusion coefficient determined by analyzing the results obtained using  ${}^4T_2$  excitation was calculated in a previous paper<sup>5</sup> assuming completely incoherent migration. Structural measurements have shown that the distribution of  $\text{Cr}^{3+}$  ions in alexandrite is not uniform.<sup>26</sup> For this reason it is difficult to determine a value for the distance between  $\text{Cr}^{3+}$  ions,  $a$ . The lower limit on  $a$  is 0.27 nm, which is the smallest distance between  $\text{Cr}^{3+}$  ions in mirror sites. For a uniform distribution of  $\text{Cr}^{3+}$  ions the value of  $a$  is 2.99 nm. Assuming a dipole-dipole interaction between  $\text{Cr}^{3+}$  ions and using the calculated ion-ion interaction rate listed in Table I, the value of  $a$  is estimated to be approximately 0.45 nm, which is intermediate between the nearest-neighbor and uniform distribution limits. Using the value of 0.45 nm for  $a$ , the magnitudes of  $D$ ,  $L_m$ , and  $L_d$ , listed in Table I, are obtained.

It was reported previously<sup>5</sup> that the temperature dependence of  $D$  is  $T^{-1/2}$  for  $T \leq 150$  K. The temperature dependence of  $\alpha$  is  $T^{0.75}$ , and  $V$  decreases slightly with temperature up to 180 K (primarily due to a slight increase in  $\Delta\nu$  in this temperature range). Using Eq. (22) and these results gives a temperature dependence of approximately  $T^{-1/2}$  for  $D$ , in agreement with the results obtained with  ${}^4T_2$  excitation. This is shown in Fig. 7.

The scattering rate depends on temperature differently for different mechanisms which limit the exciton mean free path.<sup>27</sup> The exciton scattering mechanism can be due to scattering by defects, optic phonons, or acoustic phonons. All of these processes have different temperature dependences in different limits. Scattering of excitons by acoustic phonons is the dominant scattering mechanism at low temperatures. The most general form of this type of scattering is predicted<sup>27</sup> to have a  $T^{3/2}$  temperature dependence. The smaller temperature dependence observed here may be a result of the longer-wavelength phonons not being as effective in scattering localized excitons as the shorter wavelength phonons and the difference in the electron-phonon coupling strengths for the different phonons. Long-wavelength phonons which modulate several neighboring lattice sites together are less effective in scattering excitons localized on a single lattice site than phonons which modulate neighboring sites differently.<sup>28</sup>

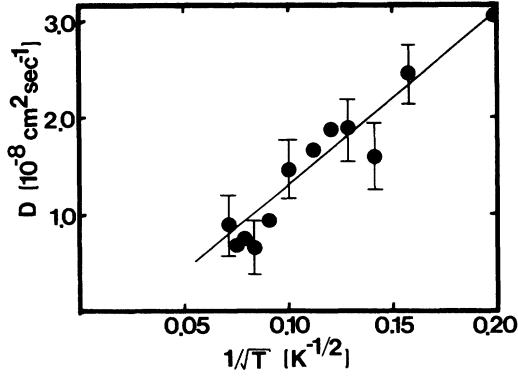


FIG. 7. Temperature dependence of the exciton diffusion coefficient for  $\text{Cr}^{3+}$  ions in the mirror sites in alexandrite obtained from values of  $V$  and  $\alpha$ . The solid line shows a  $T^{-1/2}$  dependence.

The results of the measurements of the properties of the exciton migration in alexandrite reported here are the essential characteristics needed to understand the issue of coherence in exciton migration. The term coherence in this case describes the situation in which the exciton behaves like a quasiparticle with a certain momentum. This quasiparticle will move over several lattice spacings, maintaining phase memory, before a scattering event occurs. The phase memory of the exciton does not depend upon the rest of the ensemble of excitons. Transient grating measurements have three different characteristic distances. These are the lattice constant  $a$ , the mean free path  $L_m$ , and the grating spacing  $\Lambda$ . The transport properties of the exciton are discernible using the LIG technique only if the diffusion length is comparable to half of the grating spacing, and therefore  $L_d$  and  $\Lambda$  are on the same length scale. If  $L_m$  is less than or equal to  $a$  then the exciton motion is completely incoherent and a scattering event occurs on every “hop” of the exciton to another site, leading to a complete loss of phase memory. If  $a < L_m \ll \Lambda/2$  then the exciton motion is coherent over a few lattice spacings, but is incoherent on the scale of the experiment.  $N_s$  is a measure of the degree of coherence on this length scale. If  $L_m \approx \Lambda/2$  then the exciton motion is coherent over many lattice spacings and on a distance scale which is directly discernible from the transient grating signal shapes.  $\zeta$  is a measure of the degree of coherence on this length scale. Table I shows that the mirror-site  $\text{Cr}^{3+}$  ions in alexandrite have energy transport characteristics consistent with the second type of coherence mentioned above ( $a < L_m \ll \Lambda/2$ ). The exciton motion is coherent over a few lattice spacings, but is incoherent on the distance scale of the grating, and is thus termed quasicohherent.

The coherence parameter is an important quantity in verifying the assumption mentioned earlier regarding the initial conditions of the experiment. Kenkre<sup>29</sup> has shown that for  $\zeta$  greater than 2.0 significant differences in the transient grating decay kinetics are possible depending on the initial state of the density matrix. Table I shows that  $\zeta$  is  $3.7 \times 10^{-3}$ . Therefore even if the initial density ma-

trix were not diagonal, as assumed here, there would be no difference in the transient grating decay kinetics. The LIG signal in this system is insensitive to the initial conditions of the density matrix.

#### IV. DEPHASING MEASUREMENTS

In a previous paper<sup>5</sup> it was shown that measurements of the FWM signal intensity as a function of the crossing angle between the write beams can be used to determine the dephasing time of the atomic system with respect to the laser beams. The model used to analyze the data was the model discussed in Sec. II describing the interaction between crossed laser beams and a two-level atomic system. The electric fields of the four laser beams interact with each other via the nonlinear polarization induced in the two-level system. Solving the wave equation for this situation leads to a set of coupled differential equations for the complex amplitudes of the fields. Using this approach it was found that the normalized FWM scattering efficiency could accurately be modeled by solving these equations numerically, treating the real and imaginary components of the coupling parameters,  $D_1^r$ ,  $D_1^i$ ,  $D_2^r$ , and  $D_2^i$ , as adjustable parameters. The values of the coupling parameters obtained by these computer fits to the data yielded information on the laser-induced modulation of the real and imaginary parts of the refractive index through the relationships

$$\Delta\alpha_{ss} = -2\alpha D_2^i / D_1^i, \quad (30)$$

$$\Delta n_{ss} = (\alpha c / \omega) D_2^r / D_1^i. \quad (31)$$

From these quantities the dephasing time of the atomic system,  $T_2$ , can be calculated using

$$T_2 = (2\omega/c)(\Delta n_{ss}/\Delta\alpha_{ss})(\omega - \omega_{21})^{-1} \quad (32)$$

where  $\alpha$  is the absorption coefficient at the write-beam wavelength,  $c$  is the speed of light,  $\omega$  is the circular frequency of the write beams, and  $\omega_{21}$  is the resonant frequency of the atomic transition.

There are several mechanisms that could be responsible for the dephasing of the system. The measured dephasing time is related to population relaxation  $T_1$  and phase disrupting processes among the ions of the ensemble,  $T_2^{\text{PD}}$ , by the relation<sup>30</sup>

$$T_2^{-1} = \frac{1}{2}T_1^{-1} + (T_2^{\text{PD}})^{-1}. \quad (33)$$

Population relaxation processes contribute to the total dephasing rate since they are incoherent spontaneous processes.  $T_2^{\text{PD}}$  can be separated into two parts:

$$(T_2^{\text{PD}})^{-1} = (T_2^*)^{-1} + (T_2')^{-1}, \quad (34)$$

where  $T_2^*$  is the inhomogeneous dephasing time and  $T_2'$  is the homogeneous dephasing time. These dephasing times are related to their respective contribution to the total linewidth through the relations

$$T_2^* = (\pi c \Delta\nu^*)^{-1} \quad (35)$$

and

$$T_2' = (\pi c \Delta\nu')^{-1}. \quad (36)$$

$T_2^*$  represents the time for the loss of phase coherence between the ions of the ensemble due to small mismatches in the transition energies of the ions.  $T_2'$  represents the time for the loss of coherence between the ions of the ensemble due to phonon scattering processes.<sup>22</sup>

### A. Results for ${}^2E$ excitation

Figure 8 shows the angular dependence of the normalized FWM scattering efficiency for excitation of the  $2\bar{A}$  sublevel of the  ${}^2E$  state at 50 K. The solid line in the figure is the computer fit to the data using the procedure discussed above. The parameters calculated from this fit using Eqs. (30)–(32) are listed in Table II.

For this excitation the total population relaxation is the sum of two processes:

$$T_1^{-1} = T_1^{-1}(2\bar{A}-\bar{E}) + T_1^{-1}({}^2E-{}^4A_2) \quad (37)$$

where  $T_1^{-1}(2\bar{A}-\bar{E})$  is the nonradiative decay rate from the upper crystal field sublevel of the  ${}^2E$  state to the lower sublevel, and  $T_1^{-1}({}^2E-{}^4A_2)$  is the total decay rate from the  $2\bar{A}$  and  $\bar{E}$  sublevels of  ${}^2E$  to the ground state,  ${}^4A_2$ .  $T_1^{-1}({}^2E-{}^4A_2)$  is measured<sup>11</sup> to be 2.3 ms at 50 K, and therefore this term in Eq. (37) can be neglected since it is much smaller than the measured dephasing rate of 55 ps. The nonradiative decay time from  $2\bar{A}$  to  $\bar{E}$ ,  $T_1(2\bar{A}-\bar{E})$ , has been measured by Meltzer *et al.*<sup>31</sup> at 1.5 K to be 400 ps. This decay time will decrease as temperature is raised, and can be extrapolated to its value at 50 K using the relation

$$T_1^{-1}(50 \text{ K}) = T_1^{-1}(0 \text{ K})(\bar{n} + 1) \quad (38)$$

where  $n$  is the phonon occupation number given by

$$\bar{n} = [\exp(\Delta E/k_B T) - 1]^{-1}, \quad (39)$$

$k_B$  is Boltzmann's constant and  $\Delta E$  is the phonon energy. This gives a value of 260 ps for  $T_1(2\bar{A}-\bar{E})$  at 50 K. This is a factor of 5 slower than the dephasing time measured here. At 50 K the homogeneous linewidth is less than the

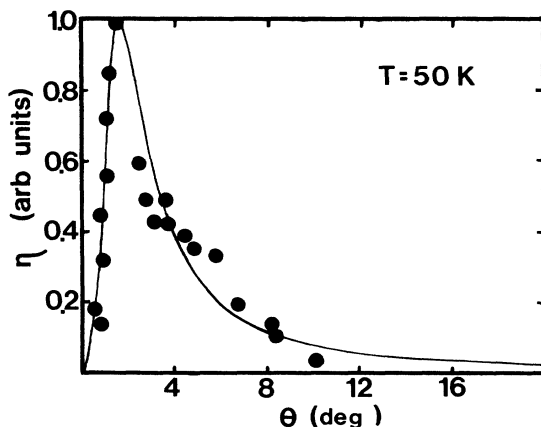


FIG. 8. Normalized FWM scattering efficiency vs the write-beam crossing angle at 50 K for  $\text{Cr}^{3+}$  ions in the mirror sites directly excited in the  $2\bar{A}$  sublevel of the  ${}^2E$  state. The solid line is the computer-generated fit obtained for a two-level atomic system model for FWM (Refs. 5 and 15).

TABLE II. Dephasing parameters.

$\lambda_{\text{exc}}$ (nm)	677.8
$T$ (K)	50
$D_1'$	0.25
$D_1''$	0.65
$D_2'$	0.35
$D_2''$	0.0015
$\Delta n$	$6.68 \times 10^{-6}$
$\Delta\alpha$ ( $\text{cm}^{-1}$ )	$4.00 \times 10^{-3}$
$T_2$ (ps)	55.3

inhomogeneous linewidth, which is approximately  $2 \text{ cm}^{-1}$ .<sup>11</sup> Therefore  $T_2^*$  is less than  $T_2'$ , and the dephasing rate is dominated by the inhomogeneous dephasing. Using Eq. (41) and the measured inhomogeneous linewidth, the inhomogeneous dephasing time is found to be 52 ps. This is in good agreement with the measured result; thus the dephasing mechanism in this case is attributed to dephasing associated with the inhomogeneous linewidth and not population relaxation.

### B. Results for ${}^4T_2$ excitation

For excitation into the  ${}^4T_2$  level,  $T_2$  was found previously<sup>5</sup> to be 80 and 2.2 ps for the inversion sites and mirror sites, respectively and the dephasing time was attributed to the nonradiative decay from the  ${}^4T_2$  level to the  ${}^2E$  metastable level. These measurements have been extended to temperatures ranging from 30 to 300 K and several different excitation wavelengths. The dephasing time was found to be constant over this temperature range, while the frequency dependence of the dephasing time was found to vary approximately as  $\omega$  on the high-energy side of the transition peak.

The dynamics of nonradiative decay processes are important in gaining a full understanding of dephasing and the role that phonons play in the dephasing process. In this section a model is presented to describe the second type of dephasing, and it is related to the dephasing results obtained for  ${}^4T_2$  excitation of the mirror-site ions.

Figure 9 shows the model used to analyze the dynamics of the mirror-site  $\text{Cr}^{3+}$  ions. The  ${}^2E$  curve actually represents four potential energy curves, and the  ${}^4T_2$  curve represents twelve potential energy curves.<sup>32</sup> This is a result of the splittings of the sublevels of each state. The  ${}^2T_1$  level has been omitted since it does not play a significant role in the nonradiative decay processes.<sup>33–35</sup> Optical absorption occurs from the ground state,  ${}^4A_2$ , to an excited vibrational level of the  ${}^4T_2$  level, represented by the vertical line in the figure. The ion is excited into an excited vibrational level of the  ${}^4T_2$  state. Following absorption, the ion relaxes very quickly to the metastable  ${}^2E$  level. This process can occur in two ways. The first mechanism is one in which the ion remains in the  ${}^4T_2$  level and emits phonons, termed internal conversion (IC), until its energy coincides with the crossing of the two excited-state adiabatic potential-energy curves, the  ${}^2E$  and  ${}^4T_2$  levels. At this energy, the relaxation process crosses over to the  ${}^2E$  level, called intersystem crossing (ISC), and the ion continues to emit phonons until the

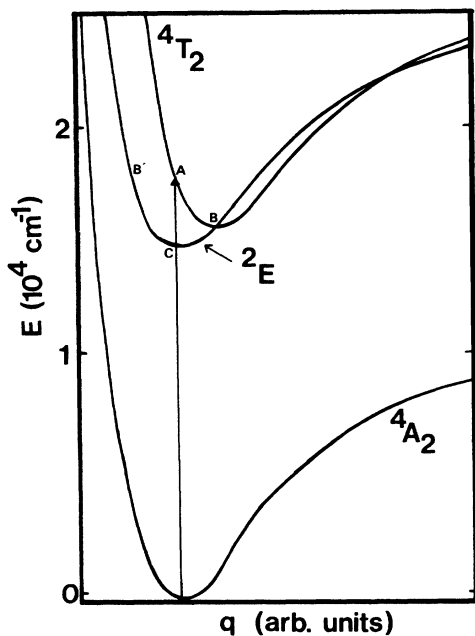


FIG. 9. Model used to analyze the dynamics of the nonradiative decay from the  $4T_2$  level to the  $2E$  level. The solid vertical line represents optical absorption.

bottom of the  $2E$  potential energy curve is reached. This is represented by the path  $A-B-C$  in Fig. 9. The second mechanism differs from the first in the point at which the ISC process occurs. In this mechanism the ISC process occurs on the very first step of the relaxation and is followed by the emission of phonons until the bottom of the  $2E$  potential energy curve is reached. The relaxation predominantly occurs in the  $2E$  electronic state, and is represented by the  $A-B'-C$  path in Fig. 9. These two mechanisms will be designated as IC and ISC, respectively, corresponding to the first steps in the relaxation mechanism.

Nonradiative decay processes occur between nonstationary states of the system.<sup>32</sup> The initial state of the system, as well as the others, is not a pure  $4T_2$  electronic state.<sup>35</sup> It is actually a mixed state of several electronic vibrational states including the  $4T_2$  and  $2E$  electronic-vibrational states. This is a result of the electron-phonon coupling, the spin-orbit interaction, and the anharmonic potential energy of the excited states of the  $Cr^{3+}$  ions. The various electronic states admixed by these interactions are shown in Fig. 10. Englman *et al.*<sup>36</sup> have shown in the harmonic approximation that the amount of admixture between the  $2E$  and  $4T_2$  states, which form the initial vibronic eigenstate of the system, can increase significantly as the vibrational quantum number of the upper state increases. Including anharmonic effects can increase the amount of admixture between states even more.

In the model used here to analyze the nonradiative decay pathways from the  $4T_2$  state to the  $2E$  state, only single-phonon processes are considered. The initial level of the system after optical excitation is an excited vibra-

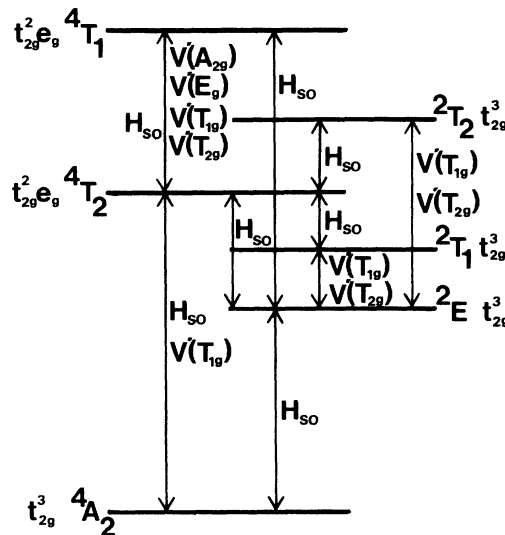


FIG. 10. Coupling scheme for the different energy levels of a  $Cr^{3+}$  ion in an octahedral environment.

tional level of the  $4T_2$  electronic state. The interactions shown in Fig. 10 admix this state with various intermediate states. From these admixed states relaxation can occur to the vibrational level of the  $4T_2$  state lying just below the initially excited level or to an excited vibrational level of the  $2E$  state which is at or below the energy of the initial level. The amount of admixture between states which causes the radiationless relaxation processes decreases as the vibrational quantum number of the initial state of the  $4T_2$  electronic state decreases.<sup>36</sup> The first step of the relaxation process is very important in determining the relaxation pathway because the amount of admixture between states which results in a specific relaxation pathway decreases after each step in the nonradiative decay process. Therefore, once the first step occurs, the pathway is determined until points are reached where there is a significant change in the admixture between states, such as at the potential-energy curve crossing points.

The nonradiative decay rate is given by the golden rule:

$$K_{nr} = (2\pi/\hbar) |\langle \Psi_{e'v'} | \Delta H | \Psi_{ev} \rangle|^2 \rho(E_f), \quad (40)$$

where  $e$  denotes the electronic part and  $v$  denotes the vibrational part of the wave function  $\Psi$ , primes denote the initial state of the system,  $\Delta H$  is the perturbation connecting the two levels, and  $\rho(E_f)$  is the density of final states. The admixture between states is accounted for in the terms retained in  $\Delta H$ , where

$$\Delta H = V'q + H_{s.o.} \quad (41)$$

Here  $q$  is the configuration coordinate representing the symmetry adapted normal mode of the system,  $V'$  is the electron-phonon coupling term, and  $H_{s.o.}$  is the spin-orbit interaction. Phonons of different symmetry are active in coupling the different levels shown in Fig. 10. These phonon symmetries are given in parentheses after the  $V'$ . The first step in the IC mechanism is the transi-

tion from  $\Psi(^4T_2, v')$  to  $\Psi(^4T_2, v)$  where  $v' > v$ . First-order perturbation theory is not sufficient to cause this transition, and it will be necessary to use second-order perturbation theory to describe this mechanism. The first step in the ISC mechanism is the transition from  $\Psi(^4T_2, v')$  to  $\Psi(^2E, v)$ . The only operator which can connect these states is the spin-orbit coupling operator. Second-order perturbation theory must also be used to

express the matrix elements in this mechanism.

Assuming that the states involved in the transition are Born-Oppenheimer states,

$$\Psi_{ev}(r, q) = \phi_e(r, q)X_v(q) \quad (42)$$

the nonradiative decay rate for each mechanism can be written as

$$\begin{aligned} K_{nr}(\text{ISC}) = & \frac{2\pi}{\hbar} \left| \sum_v \sum_p \left[ \sum_{\Gamma, \gamma, M_s, r} \sum_{\gamma'', M_s''} \langle \phi(^4T_2, \gamma^*, M_s^*) | V' | \phi(\Gamma, \gamma, M_s) \rangle \right. \right. \\ & \times \langle \phi(\Gamma, \gamma, M_s) | H_{s.o.} | \phi(^2E, \gamma'', M_s'') \rangle \langle X(^4T_2, v'_p) | q_p | X(\Gamma, r_p) \rangle \\ & \times \prod_a \langle X(^4T_2, v'_a) | X(\Gamma, r_a) \rangle \\ & \left. \left. \times \langle X(\Gamma, r_a) | X(^2E, v_a) \rangle / [W(^4T_2) - W(\Gamma)] + \text{c.c.} \right] \right|^2 \rho(E_f) \\ & + \frac{2\pi}{\hbar} \left| \sum_v \sum_p \left[ \sum_{\Gamma, \gamma', M_s', r} \sum_{\gamma'', M_s''} \langle \phi(^4T_2, \gamma^*, M_s^*) | H_{s.o.} | \phi(\Gamma', \gamma', M_s') \rangle \right. \right. \\ & \times \langle \phi(\Gamma', \gamma', M_s') | V' | \phi(^2E, \gamma'', M_s'') \rangle \langle X(\Gamma', r_p) | q_p | X(^2E, v_p) \rangle \\ & \times \prod_a \langle X(^4T_2, v'_a) | X(\Gamma', r_a) \rangle \\ & \left. \left. \times \langle X(\Gamma', r_a) | X(^2E, v_a) \rangle / [W(^2E) - w(\Gamma')] + \text{c.c.} \right] \right|^2 \rho(E_f) \quad (43) \end{aligned}$$

and

$$\begin{aligned} K_{nr}(\text{IC}) = & \frac{2\pi}{\hbar} \left| \sum_v \sum_p \left[ \sum_{\Gamma, \gamma, M_s, r} \sum_{\gamma'', M_s''} \langle \phi(^4T_2, \gamma^*, M_s^*) | V' | \phi(\Gamma, \gamma, M_s) \rangle \right. \right. \\ & \times \langle \phi(\Gamma, \gamma, M_s) | H_{s.o.} | \phi(^4T_2, \gamma'', M_s'') \rangle \langle X(^4T_2, v'_p) | q_p | X(\Gamma, r_p) \rangle \\ & \times \prod_a \langle X(^4T_2, v'_a) | X(\Gamma, r_a) \rangle \\ & \left. \left. \times \langle X(\Gamma, r_a) | X(^2E, v_a) \rangle / [W(^4T_2) - W(\Gamma)] + \text{c.c.} \right] \right|^2 \rho(E_f) \\ & + \frac{2\pi}{\hbar} \left| \sum_v \sum_p \left[ \sum_{\Gamma, \gamma', M_s', r} \sum_{\gamma'', M_s''} \langle \phi(^4T_2, \gamma^* M_s^*) | V' | \phi(\Gamma', \gamma', M_s') \rangle \right. \right. \\ & \times \langle \phi(\Gamma', \gamma', M_s') | V' | \phi(^4T_2, \gamma'', M_s'') \rangle \langle X(^4T_2, v'_p) | q_p | X(\Gamma', r_p) \rangle \\ & \times \prod_a \langle X(^4T_2, v'_a) | X(\Gamma', r_a) \rangle \\ & \left. \left. \times \langle X(\Gamma', r_a) | X(^2E, v_a) \rangle / [W(^4T_2) - W(\Gamma)] + \text{c.c.} \right] \right|^2 \rho(E_f), \quad (44) \end{aligned}$$

where  $\gamma$  represents the crystal-field component of the  $\Gamma$  intermediate state, and  $W$  is the energy of the state. The vibrational part of the wave function has been separated into promoting and accepting modes,  $X(e, v_p)$  and  $X(e, v_a)$ , respectively. These modes are assumed to be distinct, which is a good approximation for high-symmetry crystal-field sites.<sup>32</sup> Promoting modes represent phonons that mix the initial and final electronic states, and accepting modes represent phonons that absorb the difference in electronic energy. The reason for invoking admixture of intermediate states in the expres-

sion for  $K_{nr}(\text{IC})$  is due to the properties of the overlap integrals of the vibrational wave functions. The vibrational wave functions for each particular excited state are orthogonal, and therefore the vibrational overlap integral, commonly called the Franck-Condon factor, vanishes for a transition from one vibrational level to a different vibrational level of the same electronic state. Equations (43) and (44) avoid the "Condon" approximation, which tends to underestimate transition rates by as much as several orders of magnitude.<sup>33,37</sup> These expressions are summed over  $v$  and  $p$  to include all single-phonon transitions from

$v'$  to all other possible vibrational levels. There is no summation over  $v'$  because the system is initially in a specific vibrational level.

The summations in Eqs. (43) and (44) are restricted by symmetry. Figure 10 shows that for  $K_{nr}$  (ISC) and an ion in an octahedral environment  $\Gamma$  must belong to the set of states  $\{^4T_2, ^4A_2, ^4T_1\}$  and the corresponding  $V'$  must belong to the sets of vibrational symmetries  $\{\{A_{1g}, E_g, T_{1g}, T_{2g}\}, \{T_{1g}\}, \{A_{2g}, E_g, T_{1g}, T_{2g}\}\}$ . On the other hand  $\Gamma'$  must belong to the set of states  $\{^2T_1, ^2E, ^2T_2\}$  and this requires that  $V'$  must belong to the sets of vibrational symmetries  $\{\{T_{1g}, T_{2g}\}, \{A_{1g}, A_{2g}, E_g\}, \{T_{1g}, T_{2g}\}\}$ . For  $K_{nr}$  (IC)  $\Gamma$  and  $\Gamma'$  must belong to the set of states  $\{^4T_1, ^4A\}$  and the corresponding  $V'$  must belong to the set of vibrational symmetries  $\{\{A_{2g}, E_g, T_{1g}, T_{2g}\}, \{T_{1g}\}\}$ .

Measurements of the Raman spectra, low-temperature absorption spectra, and Stokes excitation spectra<sup>12</sup> show that phonons of about  $240\text{ cm}^{-1}$  are important to the dynamics of the nonradiative relaxation processes from the  $^4T_{2g}$  to  $^2E_g$  level. In octahedral symmetry there are three different species of Raman-active active modes:  $A_{1g}$ ,  $E_g$ , and  $T_{2g}$ . Symmetry assignments of the different Raman

$$\langle (t_{2g}^n)(e_g^m)S\Gamma M\gamma | V_\gamma(\Gamma) | (t_{2g}^{n'})S'\Gamma' M'\gamma' \rangle$$

$$= \delta(S, S')\delta(M, M')(\bar{\Gamma})^{-1/2} \langle \Gamma\gamma | \Gamma'\gamma'\Gamma\gamma \rangle \langle (t_{2g}^n)(e_g^m)S\Gamma || V(\Gamma) || (t_{2g}^{n'})S'\Gamma' \rangle \quad (45)$$

where  $\bar{\Gamma}$  is the dimension of the  $\Gamma$  representation,  $\delta(S, S')$  is the Kronecker delta,  $\langle \Gamma\gamma | \Gamma'\gamma'\Gamma\gamma \rangle$  is the Clebsch-Gordan coefficient, and

$$\langle (t_{2g}^n)(e_g^m)S\Gamma || V(\Gamma) || (t_{2g}^{n'})S'\Gamma' \rangle$$

is the multielectron reduced matrix element. This reduced matrix element can be reexpressed in terms of the single-electron reduced matrix elements,  $\langle t_{2g} || V(\Gamma) || t_{2g} \rangle$ ,  $\langle e_g || V(\Gamma) || e_g \rangle$ , and  $\langle t_{2g} || V(\Gamma) || e_g \rangle$ , by using the  $d$  wave functions for each representation. These wave functions are denoted  $T_{2g}(\xi, \eta, \zeta)$ ,  $T_{1g}(\alpha, \beta, \gamma)$ ,  $E_g(u, v)$ ,  $A_{2g}(e_2)$ , and  $A_{1g}(e_1)$ .<sup>41</sup>

The spin-orbit matrix elements are more complicated. The spin-orbit term in the Hamiltonian can be expressed as<sup>41</sup>

$$\begin{aligned} H_{s.o.} = & (1/\sqrt{2})[-V_{1\alpha}(1T_1) + iV_{1\beta}(1T_1)] \\ & + (1/\sqrt{2})[V_{-1\alpha}(1T_1) + iV_{-1\beta}(1T_1)] \\ & + V_{0\gamma}(1T_1), \end{aligned} \quad (46)$$

where  $V_{1\alpha}(1T_1)$  transforms as the  $\alpha$  wave function of the  $T_1$  representation with spin quantum number  $+1$ . Using the Wigner-Eckart theorem, the matrix elements of the spin-orbit interaction can be expressed in terms of the multielectron reduced matrix elements. These multielectron reduced matrix elements can also be expressed in terms of the single-electron reduced matrix element  $\langle t_{2g} || V(1T_1) || e_g \rangle$  and the results have been tabulated by Tanabe *et al.*<sup>41</sup> Table III gives the average of the matrix elements squared in terms of the single-electron reduced matrix elements after summing over the different components of the intermediate representations.

peaks seen in experiments have been done for the actual symmetry class of the mirror-site ions in alexandrite.<sup>38</sup> These can be correlated with the symmetries of the Raman-active modes in  $O_h$  point-group symmetry.<sup>39</sup>  $O_h$  symmetry is a good approximation to the actual site symmetry, and its simplification makes the calculations much easier. These measurements and this correlation show that the  $240\text{-cm}^{-1}$  phonons have  $T_{2g}$  symmetry. Thus, as a further simplification, it will be assumed that these  $240\text{-cm}^{-1}$  phonons of  $T_{2g}$  symmetry are the only phonons active in the nonradiative relaxation process. This eliminates many of the terms that would have appeared in Eqs. (43) and (44). The sum over promoting modes and the product over accepting modes are removed, leaving just one term each.

The electronic matrix elements can be reduced to single-electron matrix elements which can then be evaluated by using  $d$ -electron wave functions.<sup>40-42</sup> The matrix elements are summed over the final states and the matrix elements squared are then averaged over the initial electronic states. The matrix elements can be expressed using the Wigner-Eckart theorem as<sup>41</sup>

Nonradiative decay rates in a diatomic molecule can be affected to a large extent by anharmonic effects.<sup>43</sup> This should also be true in solids.<sup>44</sup> The exact form of the anharmonic potential energy surface for an ion in a solid is not known, but the potential can be approximated by using the well-known Morse potential. This is given by<sup>45</sup>

$$U(q) = D_0 \{1 - \exp[-a''(q - q_0)]\}^2, \quad (47)$$

where  $q$  is the configuration coordinate,  $q_0$  is the equilibrium position,  $a''$  is the anharmonicity constant, and  $D_0$  is the dissociation energy. The normalized vibrational wave functions for this type of potential are<sup>46-49</sup>

$$\begin{aligned} X_v = & [(a''b_0)(v!)/\Gamma(K - v)]^{1/2} \\ & \times \exp(-z/2)(z^{b_0/2})L_v^{b_0}(z), \end{aligned} \quad (48)$$

where

$$z = k \exp[-a''(q - q_0)], \quad (49)$$

$$K = v_e/v_e x_e = 4D_0/v_e, \quad (50)$$

$$b_0 = K - 2v - 1. \quad (51)$$

$L_v^{b_0}(z)$  is the associated Laguerre polynomial, and  $\Gamma$  is the gamma function. The vibrational energy is given by<sup>45</sup>

$$E_v = v_e(v + \frac{1}{2}) - v_e x_e(v + \frac{1}{2})^2. \quad (52)$$

This type of potential can be used to model the ground

TABLE III. Squared matrix elements;  $X = \langle t_{2g} \| V' t_{2g} \| t_{2g} \rangle$ ,  $Z = \langle e_g \| V(1t_1) \| t_{2g} \rangle$ .

		$K_{nr}$ (ISC)
$\gamma^*$	$M_s^*$	$\left  \sum_{\gamma, M_s} \sum_{\gamma'', M_s''} \langle \phi(^4T_2 \gamma^* M_s^*)   V'(T_{2g})   \phi(^4T_2 \gamma M_s) \rangle \right. \\ \left. \times \langle \phi(^4T_2 \gamma M_s)   H_{s.o.}   \phi(^2E \gamma'' M_s'') \rangle \right ^2$
$\xi$	3/2	0
	1/2	(1/486)(XZ) <sup>2</sup>
	-1/2	(1/486)(XZ) <sup>2</sup>
	-3/2	0
$\eta$	3/2	(1/2592)(1 + $\sqrt{3}$ ) <sup>2</sup> (XZ) <sup>2</sup>
	1/2	(1/3888)(14 + 5 $\sqrt{3}$ )(XZ) <sup>2</sup>
	-1/2	(1/1296)(2 - $\sqrt{3}$ )(XZ) <sup>2</sup>
	-3/2	(1/2592)(1 + $\sqrt{3}$ ) <sup>2</sup> (XZ) <sup>2</sup>
$\xi$	3/2	(1/2592)(1 + $\sqrt{3}$ ) <sup>2</sup> (XZ) <sup>2</sup>
	1/2	(1/7776)(1 + $\sqrt{3}$ ) <sup>2</sup> (XZ) <sup>2</sup>
	-1/2	(1/7776)(1 + $\sqrt{3}$ ) <sup>2</sup> (XZ) <sup>2</sup>
	-3/2	(1/2592)(1 + $\sqrt{3}$ ) <sup>2</sup> (XZ) <sup>2</sup>
$\gamma^*$	$M_s^*$	Average = (1/2916)(4 + $\sqrt{3}$ )(XZ) <sup>2</sup> $\left  \sum_{\gamma, M_s} \sum_{\gamma'', M_s''} \langle \phi(^4T_2, \gamma^*, M_s^*)   V'(T_{2g})   \phi(^4T_1, \gamma, M_s) \rangle \right. \\ \left. \times \langle \phi(^4T_1, \gamma, M_s)   H_{s.o.}   \phi(^2E, \gamma'', M_s'') \rangle \right ^2$
$\xi$	3/2	(1/384)(XZ) <sup>2</sup>
	1/2	(1/3456)(XZ) <sup>2</sup>
	-1/2	(1/3456)(XZ) <sup>2</sup>
	-3/2	(1/384)(XZ) <sup>2</sup>
$\eta$	3/2	(1.576)(2 - $\sqrt{3}$ )(XZ) <sup>2</sup>
	1/2	(1/1728)(2 + $\sqrt{3}$ )(XZ) <sup>2</sup>
	-1/2	(1/576)(2 + $\sqrt{3}$ )(XZ) <sup>2</sup>
	-3/2	(1/576)(2 + $\sqrt{3}$ )(XZ) <sup>2</sup>
$\xi$	3/2	(1/1152)(XZ) <sup>2</sup>
	1/2	(1/3456)(7 + 4 $\sqrt{3}$ )(XZ) <sup>2</sup>
	-1/2	(1/3456)(7 + 4 $\sqrt{3}$ )(XZ) <sup>2</sup>
	-3/2	(1/1152)(XZ) <sup>2</sup>
$\gamma^*$	$M_s^*$	Average = (1/2592)(5 + $\sqrt{3}$ )(XZ) <sup>2</sup> $\left  \sum_{\gamma', M_s'} \sum_{\gamma'', M_s''} \langle \phi(^4T_2, \gamma^*, M_s^*)   H_{s.o.}   \phi(^2T_1, \gamma', M_s') \rangle \right. \\ \left. \times \langle \phi(^2T_1, \gamma', M_s')   V'(T_{2g})   \phi(^2E, \gamma'', M_s'') \rangle \right ^2$
		Vanishes for all $\gamma^*, M_s^*$
$\gamma^*$	$M_s^*$	$\left  \sum_{\gamma', M_s'} \sum_{\gamma'', M_s''} \langle \phi(^4T_2 \gamma^*, M_s^*)   H_{s.o.}   \phi(^2T_2 \gamma', M_s') \rangle \right. \\ \left. \times \langle \phi(^2T_2 \gamma', M_s')   V'(T_{2g})   \phi(^2E, \gamma'', M_s'') \rangle \right ^2$
$\xi$	3/2	0
	-1/2	(1/324)(2 + $\sqrt{3}$ )(XZ) <sup>2</sup>
	-3/2	(1/324)(2 + $\sqrt{3}$ )(XZ) <sup>2</sup>
		0
$\eta$	3/2	(1/216)(XZ) <sup>2</sup>
	1/2	(1/216)(XZ) <sup>2</sup>
	-1/2	(1/648)(7 - 4 $\sqrt{3}$ )(XZ) <sup>2</sup>
	-3/2	(1/216)(XZ) <sup>2</sup>

TABLE III. (Continued).

$\xi$	3/2	$K_{nr}$ (IC)
	1/2	$(1/432)(2 + \sqrt{3})(XZ)^2$
	-1/2	$(1/1296)(2 + \sqrt{3})(XZ)^2$
	-3/2	$(1/1296)(2 + \sqrt{3})(XZ)^2$
	-3/2	$(1/432)(2 + \sqrt{3})(XZ)^2$
		Average = $(1/1944)(8 + \sqrt{3})(XZ)^2$
$\gamma^*$	$M_s^*$	$K_{nr}$ (IC)
		$\left  \sum_{\gamma', M_s'} \sum_{\gamma'', M_s''} \langle \phi(^4T_2, \gamma^*, M_s^*)   V'(T_{2g})   \phi(^4T_1, \gamma', M_s') \rangle \right. \\ \left. \times \langle \phi(^4T_1, \gamma', M_s')   H_{s.o.}   \phi(^4T_2, \gamma'', M_s'') \rangle \right ^2$
$\xi$	3/2	$(1/384)(XZ)^2$
	1/2	$(1/3456)(XZ)^2$
	-1/2	$(1/3456)(XZ)^2$
	-3/2	$(1/384)(XZ)^2$
$\eta$	3/2	$(1/576)(2 - \sqrt{3})(XZ)^2$
	1/2	$(1/1728)(2 + \sqrt{3})(XZ)^2$
	-1/2	$(1/576)(2 + \sqrt{3})(XZ)^2$
	-3/2	$(1/576)(2 + \sqrt{3})(XZ)^2$
$\zeta$	3/2	$(1/1152)(XZ)^2$
	1/2	$(1/3456)(7 + 4\sqrt{3})(XZ)^2$
	-1/2	$(1/3456)(7 + 4\sqrt{3})(XZ)^2$
	-3/2	$(1/1152)(XZ)^2$
		Average = $(1/2592)(5 + \sqrt{3})(XZ)^2$
$\gamma^*$	$M_s^*$	$\left  \sum_{\gamma', M_s'} \sum_{\gamma'', M_s''} \langle \phi(^4T_2, \gamma^*, M_s^*)   V'(T_{2g})   \phi(^4T_1, \gamma', M_s') \rangle \right. \\ \left. \times \langle \phi(^4T_1, \gamma', M_s')   V'(T_{2g})   \phi(^4T_2, \gamma'', M_s'') \rangle \right ^2$
		Vanishes for all $\gamma^*, M_s^*$

and excited states of  $\text{Cr}^{3+}$  ions in alexandrite. Figure 11 shows an approximate Morse potential energy curve for the  $^4T_2$  and  $^2E$  excited states. These curves were calculated using the absorption and fluorescence spectra, positions of the zero-phonon lines, and an effective phonon energy of  $240 \text{ cm}^{-1}$ . The energy difference between the bottom of the  $^4T_2$  and  $^2E$  potential energy curves is  $800 \text{ cm}^{-1}$ . The energy levels of the vibrational levels in each excited state calculated by using Eq. (52) are shown in the figure. Equations (48)–(51) were used to calculate the vibrational wave functions for each vibrational level in both electronic states. These are also shown in the figure.

The vibrational parts of the matrix elements in Eqs. (43) and (44) given by

$$|\langle X(^4T_2v') | X(^2Ev) \rangle|^2 \quad (53)$$

and

$$|\langle X(^4T_2v') | q_p | X(^2Ev) \rangle|^2, \quad (54)$$

etc., can be calculated by using the Morse potential wave functions.<sup>43,47,49–54</sup> The first type of matrix element is the Franck-Condon factor (FCF). The FCF cannot be calculated analytically; therefore, both types of matrix elements in Eqs. (53) and (54) were calculated numerically.

The peak in the  $^4T_2$  absorption is into the fourth vibrational level of the  $^4T_2$  state. Figure 12 shows the calcu-

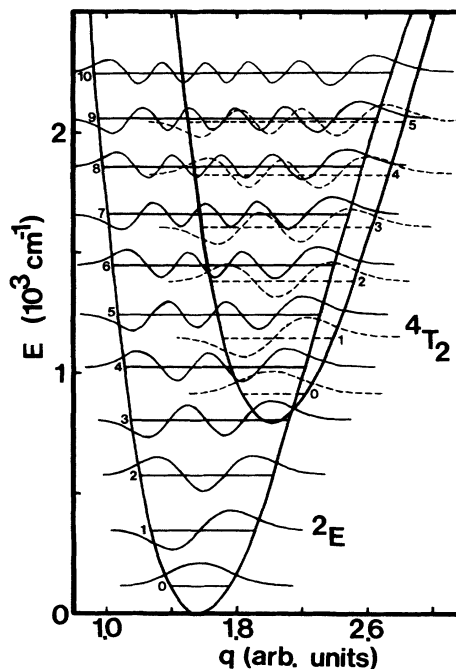


FIG. 11. Morse potentials representing the  $^4T_2$  and  $^2E$  levels of  $\text{Cr}^{3+}$  ions in mirror sites in alexandrite. The horizontal lines represent the vibrational energy levels for  $240\text{-cm}^{-1}$  phonons, and the oscillating lines represent the wave functions for each vibrational energy level.

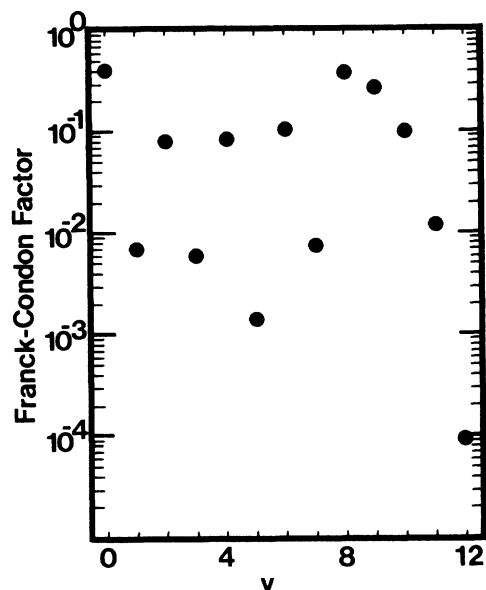


FIG. 12. Franck-Condon factors for a transition from the fourth vibrational level of the  ${}^4T_2$  state to various vibrational levels of the  ${}^2E$  state designated by vibrational quantum number  $v$ .

lated FCF from this level to each of the vibrational levels of the  ${}^2E$  state. The oscillations are a result of the alternation in sign of the wave functions. The transition from the fourth vibrational level of the  ${}^4T_2$  state to the vibrational level of the  ${}^2E$  state next lowest in energy ( $4 \rightarrow 8$ ) has a FCF of approximately 0.14. This FCF is larger than the corresponding FCF in the harmonic approximation because of the shape of the wave functions and the relative positions of the Morse potential-energy curves for large values of  $q$ . The potential-energy curves are very close to one another in this region, and the wave functions all have a large positive lobe on this side of the Morse curve. These features are shown in Fig. 11. Therefore, the overlap between vibrational wave functions is predominantly due to the overlap of these positive lobes. The shapes of the wave functions are also indicative of the anharmonicity of the potential-energy curves. The asymmetry of the wave functions is significant even for the second or third vibrational levels. For this reason it is very important to take these anharmonic effects into account.

The vibrational wave functions in a Morse potential are orthonormal. As mentioned previously, this is the reason for resorting to second-order perturbation theory in calculating  $K_{nr}(\text{IC})$ . The FCF's between the same vibrational sublevels of different electronic states having the same electronic configuration can be set equal to 1 since these potentials are essentially identical. All other FCF's between these levels are small because of orthonormality. The  ${}^2E$ ,  ${}^2T_1$ , and  ${}^2T_2$  states originate from the  $t_{2g}^3$  electronic configuration, whereas the  ${}^4T_2$  and  ${}^4T_1$  states originate from the  $t_{2g}^2 e_g$  electronic configuration. The vibrational matrix element in Eq. (54) was also calculated numerically. The same types of assumptions mentioned above were used in calculating the various matrix ele-

ments between states.

Equations (43) and (44) can be evaluated by using the results in Table III, the vibrational matrix elements, and spectroscopic data giving the energies of the levels. The reduced matrix elements can be eliminated from the equations by taking the ratio of  $K_{nr}(\text{ISC})$  to  $K_{nr}(\text{IC})$ . This avoids the problems associated with using approximate electronic wave functions to evaluate the single-electron reduced matrix elements which can severely affect the results.<sup>32</sup> Taking the ratio given the relative probability of the two processes. The vibrational matrix elements between a specific vibrational level of an electronic state and another vibrational level of the intermediate electronic state were chosen so that the ion would end up in a level of lower total energy and the calculated rate would have its maximum value. The density of states for the ISC transition was taken from the vibrational level spacing of the  ${}^2E$  Morse potential curve at the level at which the first step in the nonradiative decay process ends. The density of states for the IC transition was taken from the vibrational level spacing of the  ${}^4T_2$  Morse potential curve at the vibrational level just below the point of optical absorption. This is a result of limiting each step in the nonradiative decay mechanism to single phonon processes. There is an additional factor of  $\frac{4}{12}$  that accounts for the difference in the degeneracies in the ratio of the density of final states. The result of this calculation gives

$$\frac{K_{nr}(\text{ISC})}{K_{nr}(\text{IC})} \approx 13. \quad (55)$$

The model for nonradiative decay presented here is different from other models in several respects. The promoting mode interaction is not assumed to be effective only at or near the point where the  ${}^4T_2$  and  ${}^2E$  potential energy curves cross.<sup>32,55-57</sup> This is one of the reasons that the ISC mechanism can compete with the standard Dexter, Klick, and Russell<sup>56</sup> IC mechanism. The effects of anharmonicities, which are difficult to treat in a solid and have therefore usually been ignored in previous treatments, are included in the estimates of the FCF's and the vibrational matrix elements determined here. The harmonic approximation would lead to FCF's that are much smaller than those obtained here, and this has justified, in the past, the neglect of the ISC channel for nonradiative decay mechanism proposed here. The reason the FCF's are larger when anharmonic effects are included is due to the shape of the wave functions and the shape of the Morse potential-energy curves. The Morse curves shown in Fig. 9 actually have two crossing points, and the curves remain close together in the region between these points. This keeps the vibrational overlap integrals from decreasing to the value that would be obtained in the harmonic approximation. In the harmonic approximation the potential-energy curves cross in only one point, and the curves get farther apart as the vibrational quantum number increases above the crossing point.

Figure 13 shows the dephasing time calculated from the FWM data for  $\text{Cr}^{3+}$  ions in several different crystal-field environments, alexandrite mirror and inversion sites, emerald, and ruby. The dephasing time is shown as a

function of the energy difference between the peak of the  ${}^4T_2$  absorption and the  ${}^2E$  absorption. This energy difference is essentially the energy that must be emitted in the nonradiative decay process outlined above. The dephasing mechanism is a result of population relaxation from the  ${}^4T_2$  level. The dependence of the dephasing rate on the energy difference shown in Fig. 13 strongly supports the conclusion reached above that the dominant nonradiative decay channel is the ISC channel. If the nonradiative decay process does not involve the ISC decay channel, then the dephasing rate would not depend on the crystal field strength of the host crystal, and therefore would be independent of the energy difference between the  ${}^4T_2$  and  ${}^2E$  absorption transitions. If the ISC channel of nonradiative decay is the dominant relaxation pathway, then the well-known exponential dependence of the decay rate on the energy gap should be observed.<sup>35,38</sup> This is observed in the data, confirming the results of the theoretical calculation for the relative branching ratio of the two relaxation pathways. The dominant decay channel in other host crystals with smaller crystal field strengths and therefore a smaller energy difference between  ${}^4T_2$  and  ${}^2E$  absorption transitions may be different. An increase in the probability of the IC decay channel would decrease the ratio in Eq. (55) leading to the independence of  $T_2$  on the energy difference between the  ${}^4T_2$  and  ${}^2E$  absorption transitions.

The mechanism for dephasing in this case is consistent with a population relaxation process, namely the  ${}^4T_2$ - ${}^2E$  nonradiative decay. The temperature dependence of the dephasing rate should be the same as that of the multiphoton emission rate. The temperature dependence of the multiphoton emission rate is

$$R \approx (\bar{n} + 1)^{p'}, \quad (56)$$

where  $p'$  is the number of phonons emitted. The energy difference between the peak in the  ${}^4T_2$  and  ${}^2E$  absorption

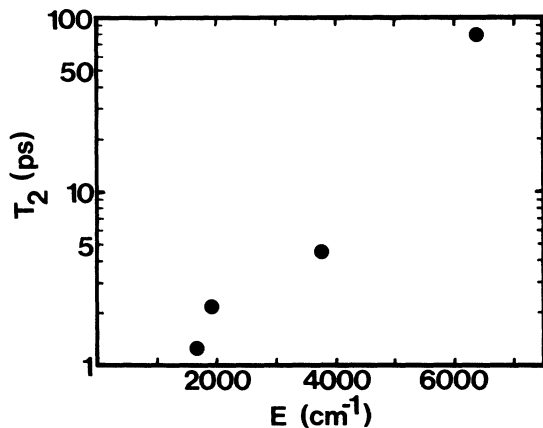


FIG. 13. Dephasing time for  $\text{Cr}^{3+}$  ions in several different crystal-field environments as a function of the energy difference between the peak in the  ${}^4T_2$  and  ${}^2E$  absorption transitions. The results were obtained for pumping in the  ${}^4T_2$  level of alexandrite inversion sites, ruby, alexandrite mirror sites, and emerald listed in decreasing order of the energy difference (adapted from data reported in Refs. 5 and 6).

transitions for the mirror site  $\text{Cr}^{3+}$  ions is  $1900 \text{ cm}^{-1}$ . Measurements of the vibronic, Raman, and anti-Stokes excitation spectra<sup>12</sup> have shown that the phonons of lowest energy for which the electron-phonon coupling is significant are  $240\text{-cm}^{-1}$  phonons.  $40\text{-cm}^{-1}$  phonons play an important role in the dynamics of the  ${}^2E$  state,<sup>31</sup> but should not be as important in the  ${}^4T_2$ - ${}^2E$  nonradiative decay. This leads to a multiphonon emission rate at 300 K that is only slightly higher than the multiphonon emission rate at 30 K. This agrees with the experimental observations within the experimental error.

### C. FWM signal intensity

The intensity of the FWM signal for excitation into the  ${}^2E$  and  ${}^4T_2$  levels was measured under identical conditions: temperature (50 K), grating spacing, power, and polarization. The measured value of the signal intensity was adjusted to account for the difference in the absorption coefficient at the two excitation wavelengths. The results show that the FWM signal formed after direct excitation into the  ${}^2E$  state is 43 times more intense than the FWM signal formed after excitation into the  ${}^4T_2$  state. In both cases the grating inducing the scattering is a population grating of  $\text{Cr}^{3+}$  ions in the  ${}^2E$  level. There are two possible reasons for this. First, it has been shown here that an inversion site grating is formed after excitation into the  ${}^4T_2$  band but not after excitation into the  ${}^2E$  zero-phonon lines of the mirror-site ions. This can provide a loss mechanism which decreases the FWM signal intensity. Second, the difference in dephasing times, 2.2 and 55 ps, for the  ${}^4T_2$  and  ${}^2E$  excitations, respectively, may be the reason for this difference. The dephasing time is related to the laser-induced changes in the optical properties of the material<sup>15</sup> which are responsible for the FWM process, and therefore can indirectly affect the FWM scattering efficiency as shown in Eq. (12). Since the first process has been shown to be very weak, the second process should be the dominant cause for the difference in the scattering efficiency at the two excitation wavelengths.

## V. DISCUSSION AND CONCLUSIONS

In this paper LIG techniques have been used to extend the previously reported energy transfer and dephasing studies in alexandrite. The temperature dependence of the exciton diffusion constant is the same for excitation into the  ${}^2E$  level and for excitation into the  ${}^4T_2$  level. Using the theoretical framework developed by Kenkre,<sup>23,24</sup> the temperature dependence of the ion-ion interaction rate and exciton scattering rate have been deduced. It should be noted that the formalism of Kenkre is exact only on a perfect lattice, and thus the theory of Kenkre should be considered an approximation to the exciton dynamics of the actual system. In this system there is a broad distribution of distances between  $\text{Cr}^{3+}$  ions, and hence there is a broad distribution of interaction strengths between  $\text{Cr}^{3+}$  ions. Therefore, the ion-ion interaction strength in the Kenkre theory should be considered to be an average interaction strength. The temperature dependence of the ion-ion interaction rate is con-

sistent with the Dexter<sup>25</sup> model, dominated by the lifetime and linewidth of the spectral transition. This same analysis was used to analyze the data obtained pumping into the  ${}^4T_2$  level. The ion-ion interaction rate is the same as obtained for the  ${}^2E$  excitation, but the exciton scattering rate is slightly higher. This may be a result of the additional phonons generated in the nonradiative decay from the  ${}^4T_2$  state to the  ${}^2E$  state. This also confirms that the grating is formed in the  ${}^2E$  state. The exciton transport properties imply a nonuniform distribution of  $\text{Cr}^{3+}$  ions. The intensity of the inversion-site grating contribution to the LIG signal as a function of the grating spacing is consistent with the very low concentration of inversion-site  $\text{Cr}^{3+}$  ions in this sample. Results of similar measurements<sup>6</sup> have shown that the exciton diffusion coefficient in emerald increases with increasing temperature. For that case the exciton scattering rate was found to increase with temperature similarly to the alexandrite results, but the ion-ion interaction rate exhibited a much stronger increase with temperature. This is due to the smaller crystal-field splitting in emerald which allows the  ${}^4T_2$  level to become thermally populated at much lower temperatures than in alexandrite. The higher oscillator strength for the  ${}^4T_2$ -to- ${}^4A_2$  transition and the greater spectral overlap from the  ${}^4T_2$  emission significantly enhances the energy transfer efficiency.

The transient LIG signal was found to reflect the saturation behavior of the pumping dynamics. The model used to analyze these transients accurately predicts the functional dependence of the pumping dynamics on the lifetime of the excited state, the pump intensity, and the absorption cross section. The absorption cross section for the inversion-site ions at 488 nm and the laser-induced change in the index of refraction were calculated to be  $0.5 \times 10^{-20} \text{ cm}^2$  and  $5.0 \times 10^{-6}$ , respectively. The results of similar measurements on ions in the mirror sites are consistent with the higher value of the saturation parameter. The power dependence of the LIG signal shows a quadratic dependence at low pump powers, but at high pump powers a deviation from this dependence is evident. The analysis of the data that this departure from a quadratic dependence is not a result of a normal saturation

process in the pumping dynamics, but is a result of beam depletion through the laser-induced change in the absorption coefficient.

Measurements of the FWM scattering efficiency as a function of the grating spacing yield information on the dephasing time of the system. These measurements were done for excitation into the  ${}^2E$  and  ${}^4T_2$  states and an analysis of the data yielded two different types of dephasing mechanisms. The dephasing time for the direct excitation of the  ${}^2E$  level is consistent with the linewidth data, implying that the inhomogeneous dephasing time is the dominant dephasing mechanism. It should be noted that this is not a line narrowing experiment and specific subsets of ions are not excited. The dephasing time for excitation into the  ${}^4T_2$  band is consistent with the nonradiative decay time from the  ${}^4T_2$  level to the  ${}^2E$  level. This is also evidenced in the temperature dependence of the dephasing time. A detailed theoretical analysis of the nonradiative decay process was carried out. The model used for this analysis includes the effects of anharmonicity and the admixing of the different states of the system. The results show the importance of intersystem-crossing in the initially excited vibrational level of the  ${}^4T_2$  state. Calculation of the relative branching ratio shows this pathway for decay to the bottom of the  ${}^2E$  potential well to be more probable than the pathway leading to the initial relaxation to the bottom of the  ${}^4T_2$  potential well. The dephasing time for alexandrite, emerald and ruby was found to vary approximately exponentially with the energy gap between the peak of the  ${}^4T_2$  absorption and the  ${}^2E$  absorption, and this is interpreted as evidence for the important role this ISC relaxation pathway plays in the dephasing processes in these materials. Also, the intensities of the FWM signals for excitation into the  ${}^4T_2$  and  ${}^2E$  levels were found to be significantly different and this is attributed to the difference in the dephasing rates.

#### ACKNOWLEDGMENT

This research was supported by the U.S. Army Research Office.

\*Permanent address: Institute of Physics, Polish Academy of Sciences, Aleja Lotników 32/46, 02-668 Warsaw, Poland.

<sup>1</sup>J. R. Salcedo, A. E. Siegman, D. D. Dlott, and M. D. Fayer, *Phys. Rev. Lett.* **41**, 131 (1978).

<sup>2</sup>H. J. Eichler, J. Eichler, J. Knof, and Ch. Noack, *Phys. Status Solidi A* **52**, 481 (1979).

<sup>3</sup>D. S. Hamilton, D. Heiman, J. Feinberg, and R. W. Hellwarth, *Opt. Lett.* **4**, 124 (1979).

<sup>4</sup>P. F. Liao, L. M. Humphrey, D. M. Bloom, and S. Geschwind, *Phys. Rev. B* **20**, 4145 (1979).

<sup>5</sup>A. Suchocki, G. D. Gilliland, and R. C. Powell, *Phys. Rev. B* **35**, 5830 (1987).

<sup>6</sup>G. J. Quarles, A. Suchocki, R. C. Powell, and S. Lai, *Phys. Rev. B* (to be published).

<sup>7</sup>A. Suchocki, R. C. Powell, *Chem. Phys.* accepted for publication

<sup>8</sup>A. M. Ghazzawi, J. K. Tyminski, R. C. Powell, and J. C. Walling, *Phys. Rev. B* **30**, 7182 (1984).

<sup>9</sup>J. C. Walling, O. G. Peterson, H. P. Jenssen, R. C. Morris, and E. W. O'Dell, *IEEE J. Quantum Electron.* **QE-16**, 1302 (1980).

<sup>10</sup>R. E. Newnham, R. Santoro, J. Pearson, and C. Jansen, *Am. Mineral.* **49**, 427 (1964).

<sup>11</sup>R. C. Powell, L. Xi, X. Gang, G. J. Quarles, and J. C. Walling, *Phys. Rev. B* **32**, 2788 (1985).

<sup>12</sup>A. Suchocki, G. D. Gilliland, R. C. Powell, J. M. Bowen, and J. C. Walling, *J. Lumin.* **37**, 29 (1987).

<sup>13</sup>K. K. Shepler, *J. Appl. Phys.* **56**, 1314 (1984).

<sup>14</sup>M. L. Shand, J. C. Walling, and R. C. Morris, *J. Appl. Phys.* **52**, 953 (1981).

<sup>15</sup>R.L. Abrams and R. C. Lind, *Opt. Lett.* **2**, 94 (1978).

<sup>16</sup>A. Yariv and D. M. Pepper, *Opt. Lett.* **1**, 16 (1977).

- <sup>17</sup>J. K. Tyminski, R. C. Powell, and W. K. Zwicker, *Phys. Rev. B* **29**, 6074 (1984).
- <sup>18</sup>Y. Silberberg and I. Bar-Joseph, *IEEE J. Quantum Electron.* **QE-17**, 1967 (1981).
- <sup>19</sup>H. Fujiwara and K. Nagawa, *J. Opt. Soc. Am. B* **4**, 121 (1987).
- <sup>20</sup>J. A. Buck and J. R. Rodriguez, *J. Opt. Soc. Am. B* **4**, 1988 (1987).
- <sup>21</sup>C. M. Lawson, R. C. Powell, and W. K. Zwicker, *Phys. Rev. Lett.* **46**, 1020 (1981).
- <sup>22</sup>M. D. Fayer, in *Spectroscopy Excitation Dynamics of Condensed Molecular Systems*, edited by V. M. Agranovich and R. M. Hochstrasser (North-Holland, Amsterdam, 1983), p. 185.
- <sup>23</sup>V. M. Kenkre and D. Schmid, *Phys. Rev. B* **31**, 2430 (1985).
- <sup>24</sup>Y. M. Wong and V. M. Kenkre, *Phys. Rev. A* **22**, 3072 (1980).
- <sup>25</sup>D. L. Dexter, *J. Chem. Phys.* **21**, 836 (1953).
- <sup>26</sup>S. C. Stotlar and L. B. Edgett, in *Proceedings of the Optical Society of America Annual Meeting*, Washington, D.C., 1985 (unpublished).
- <sup>27</sup>V. M. Agranovich and M. D. Galanin, *Electronic Excitation Energy Transfer in Condensed Matter* (North-Holland, Amsterdam, 1982).
- <sup>28</sup>T. Holstein, S. K. Lyo, and R. Orbach, in *Laser Spectroscopy of Solids*, edited by W. M. Yen and P. M. Selzer (Springer-Verlag, Berlin, 1981), Chap. 2.
- <sup>29</sup>V. M. Kenkre and D. Schmid, *Chem. Phys. Lett.* **140**, 238 (1987).
- <sup>30</sup>M. D. Levenson, *Introduction to Nonlinear Laser Spectroscopy* (Academic, New York, 1982).
- <sup>31</sup>D. Boye, S. Majetich, J. E. Rives, R. S. Meltzer, and R. M. MacFarlane, *J. Lumin.* **4**, P74 (1987).
- <sup>32</sup>R. H. Bartram, J. C. Charpie, L. J. Andrews, and A. Lempicki, *Phys. Rev. B* **34**, 2741 (1986).
- <sup>33</sup>B. Z. Malkin, *Fiz. Tverd. Tela (Leningrad)* **4**, 2214 (1962) [*Sov. Phys.—Solid State* **4**, 1620 (1963)].
- <sup>34</sup>R. Englman, B. Champagnon, E. Duval, and A. Monteil, *J. Lumin.* **28**, 337 (1983).
- <sup>35</sup>R. Englman, *Nonradiative Decay of Ions and Molecules in Solids* (North-Holland, Amsterdam, 1979).
- <sup>36</sup>R. Englman and B. Barnett, *J. Lumin.* **3**, 37 (1970); B. Barnett and R. Englman, *ibid.* **3**, 55 (1970).
- <sup>37</sup>K. Huang, *Sci. Sin.* **24**, 27 (1981).
- <sup>38</sup>Jia Weiyi, Zheng Qingrong, Shang Yusheng, Wang Yanyun, Yao Zhenyi, He Shouan, Zhou Hetian, and Liu Liling, *Kexue Tongbao* **30**, 452 (1985).
- <sup>39</sup>E. B. Wilson, J. C. Decius, and P. C. Cross, *Molecular Vibrations* (Dover, New York, 1955).
- <sup>40</sup>J. S. Griffith, *The Theory of Transition Metal Ions* (Cambridge University Press, Cambridge, England, 1961).
- <sup>41</sup>S. Sugano, Y. Tanabe, and H. Kamimura, *Multiplets of Transition-Metal Ions in Crystals* (Academic, New York, 1970).
- <sup>42</sup>A. L. Schawlow, A. H. Piksis, and S. Sugano, *Phys. Rev.* **122**, 1469 (1961).
- <sup>43</sup>B. I. Makshantsev, *Opt. Spektrosk.* **31**, 355 (1971) [*Opt. Spectrosc. (USSR)* **31**, 191 (1971)].
- <sup>44</sup>M. D. Sturge, *Phys. Rev. B* **8**, 6 (1973).
- <sup>45</sup>P. M. Morse, *Phys. Rev.* **34**, 57 (1929).
- <sup>46</sup>J. A. C. Gallas, *Phys. Rev. A* **21**, 1829 (1980).
- <sup>47</sup>P. A. Fraser and W. R. Jarman, *Proc. Phys. Soc. London Sect. A* **66**, 1145 (1953); **66**, 1153 (1953).
- <sup>48</sup>V. S. Vasan and R. J. Cross, *J. Chem. Phys.* **78**, 3869 (1983).
- <sup>49</sup>J. A. C. Gallas, H. P. Grieneisen, and B. P. Chakraborty, *J. Chem. Phys.* **69**, 612 (1978).
- <sup>50</sup>T. Y. Chang and M. Karplus, *J. Chem. Phys.* **52**, 783 (1970).
- <sup>51</sup>M. Ramjee, M. L. P. Rao, D. V. K. Rao, and P. T. Rao, *J. Chem. Phys.* **75**, 1574 (1981).
- <sup>52</sup>I. I. Tugov, *Opt. Spektrosk.* **45**, 660 (1978) [*Opt. Spectrosc. (USSR)* **45**, 627 (1978)].
- <sup>53</sup>V. B. Sovkov and V. S. Ivanov, *Opt. Spektrosk.* **59**, 1222 (1985) [*Opt. Spectrosc. (USSR)* **59**, 733 (1985)].
- <sup>54</sup>B. I. Makshantsev, *Opt. Spektrosk.* **34**, 872 (1973) [*Opt. Spectrosc. (USSR)* **34**, 503 (1973)].
- <sup>55</sup>A. M. Stoneham and R. H. Bartram, *Solid-State Electron.* **21**, 1325 (1978).
- <sup>56</sup>D. L. Dexter, C. C. Klick, and G. A. Russell, *Phys. Rev.* **100**, 603 (1955).
- <sup>57</sup>R. H. Bartram and A. M. Stoneham, *Semicond. Insulators* **5**, 297 (1983).
- <sup>58</sup>R. Englman and J. Jortner, *Mol. Phys.* **18**, 145 (1970).